



# The bar-resonator interaction in mallet percussion instruments: A multi-modal model and experimental validation

Filipe Soares <sup>a,\*</sup>, Vincent Debut <sup>a,b</sup>, Jose Antunes <sup>a</sup>

<sup>a</sup> Instituto Superior Técnico – Centro de Ciências e Tecnologias Nucleares, Lisboa, Portugal

<sup>b</sup> Instituto Politécnico de Castelo Branco – Escola de Artes Aplicadas, Castelo Branco, Portugal

## ARTICLE INFO

### Keywords:

Bar-resonator interaction  
Vibro-acoustic coupling  
Multi-modal  
Experimental validation  
Marimba  
Vibraphone

## ABSTRACT

In some mallet percussion instruments, like vibraphones and marimbas, acoustical resonators are placed under the tuned bars to enhance acoustic radiation. Despite its wide use in commercial instruments, the vibro-acoustic interaction between the tuned bars and their acoustic resonators has not been studied extensively, and previous modeling attempts often neglect important aspects of the coupling dynamics. This work presents a physical model describing the two-way vibro-acoustic interaction between a vibrating beam and an acoustic resonator. The proposed formulation leads to a system composed of a set of mechanical oscillators coupled to a set of acoustical oscillators, representing bar and resonator modes, respectively. The simplicity of the proposed model provides an intuitive understanding of the physics occurring in real instruments and show how specific design parameters will affect their behavior. The dynamics of the system are analyzed through energy balance, time-domain simulations and eigenvalue analysis, revealing a number of interesting features and highlighting three dimensionless parameters: the ratio of frequencies and quality factors, as well as a coupling “strength” coefficient, dependent on the bar-resonator distance, the placement of the resonator along the bar length, bar and resonator mode shapes, amongst others. The proposed model is also shown to be a useful tool for the design of instruments optimized for multi-modal coupling, where several resonator modes are tuned to bar frequencies. Finally, experimental results are presented to validate various aspects of the proposed model and demonstrate its capacity to emulate real instruments, both qualitatively and quantitatively.

## 1. Introduction

Mallet percussion instruments (e.g. marimba, vibraphone, xylophone, etc.) are composed of a series of tuned bars that, once struck by a mallet, vibrate and radiate sound at their natural frequencies of vibration. Generally, the tuning of the bars is achieved by removing material from the bar underside such that the first few modal frequencies become harmonically aligned (multiple integers of the fundamental frequency). In most commercial instruments, the frequencies of the first three vertical-bending modes are generally tuned. Yet, recent years have seen a number of studies [1–4] using optimization algorithms to find undercut geometries that lead to the tuning of many bar modes to a set of predefined target frequencies. Moreover, some studies considered the tuning of non-vertical-bending modes (torsional, lateral) in parallel with vertical-bending modes [5,6]. Experimental validation of optimized

\* Corresponding author.

E-mail address: [filiipe.soares@ctn.tecnico.ulisboa.pt](mailto:filiipe.soares@ctn.tecnico.ulisboa.pt) (F. Soares).

bars [6,7] has demonstrated the potential of such methods, leading to bars with demanding tuning ratios (up to six target frequencies) at absolute tuning deviations typically below 10–15 cents.

In some instruments, resonator pipes are placed under the vibrating bars to enhance sound radiation. Most often, these resonators are pipes of uniform cross-section, closed at the bottom end and open at the top. Early experimental reports by Bork [8] have demonstrated that when the fundamental frequency of the acoustic resonator is aligned with that of a bar mode, the two (mechano-acoustic) elements experience a vibro-acoustic coupling, which generally leads to an increase of sound radiation. On the other hand, the increased sound radiation is often accompanied by a proportional decrease of the bar decay time.

In most commercial instruments, where tuning ratios of bars are typically (1:4:10), only the fundamental acoustic mode of the resonator will have a meaningful interaction with the bar vibration, and sound radiation will be enhanced only at the fundamental frequency. However, we underline the work of Henrique et al. [9,10], that have developed methods to design resonators with natural frequencies tuned to a set of pre-defined targets, such that bars and resonators could have matching modal frequencies, potentially leading to increased acoustic radiation at multiple frequencies. These studies provide an exciting impulse for the development of improved instruments.

Despite the advances on the design optimization of the individual elements (bars and resonators), the nature of the vibro-acoustic coupling between the two has not been studied extensively. One of the first modeling efforts was made by Chaigne and Doutaut [11,12], where bar vibrations and sound radiation are calculated in the presence of acoustic resonators. However, their model assumes coupling in only one way, i.e. it neglects the back-coupling effect of the resonator on the bar vibration. This is in contradiction with experimental observations, which report significant changes to bar decay time when a tuned resonator is present [8]. More recently, the work published by Rucz et al. [13] deals with the use of 3-D finite element (FE) models to describe the (two-way) vibro-acoustic interaction as well as the sound pressure radiated into the free-field. Here, the 3-D structural (bar) and acoustical domains (resonator and free field) are decomposed into a 3-D vibro-acoustic modal basis, which is then used to perform temporal integrations of the coupled system. Although undeniably useful for realistic sound synthesis, approaches of this type (using 3-D FE models) entail large computational costs and are less practical for parametric studies. In this context, simplified modeling approaches may be useful tools in underlining the main dimensionless parameters influencing the instruments' behavior and providing guidelines for the design/-optimization of real instruments.

In recent work by the authors [14,15], a minimal model for the vibro-acoustic interaction was developed, in an effort to better understand the underlying physics and provide a basis for a simplified modeling framework. To this end, a single bar mode was represented by a disk-shaped oscillator, while the acoustics of a cylindrical resonator (of the same radius) were described in a modal framework. The vibro-acoustic transfer function between the two elements was calculated by a 2-D axisymmetric finite element model, whose numerical results were then fitted to dimensionless analytical expressions. Finally, the interaction between a single bar and resonator modes was reduced to a system of two coupled oscillators. Despite its simplifications, the model was able to accurately reproduce the dynamical behavior observed in experimental reports.

This work presents a generalization of previous modeling efforts, now including the interaction between an actual bar and an acoustic resonator. The proposed formulation leads to a dynamical system describing the interaction between a set of mechanical oscillators (bar modes) coupled to a set of acoustic oscillators (resonator modes). The simplicity of the resulting system provides an intuitive understanding of the dynamics found in real instruments and how specific design parameters will affect their behavior. Namely, when considering the coupling between a generic bar and resonator modes, three dimensionless parameters emerge from the formulation: the ratio of frequencies and quality factors as well as a coupling “strength” coefficient, dependent on the bar resonator distance, the placement of the resonator along the bar length, the bar and resonator mode shapes, amongst others. Additionally, the proposed model is a practical tool in the advent of designing optimized instruments with multi-modal coupling where several resonator modes are in tune with bar frequencies.

In Section 2 the proposed model is derived, eventually reaching a multi-modal formulation. In Section 3 we analyze a simplified version of the model, consisting of the coupling between one generic bar mode and one generic resonator mode. In Section 4, temporal integrations are used to compare the behavior of a typical instrument with cylindrical resonators, to that of an optimized instrument, where multiple resonator modes are tuned to bar frequencies. Finally, experimental validation of the proposed model is presented in Section 5.

## 2. Model description

In this model, we consider the coupling dynamics between a free-free vibrating beam and a cylindrical acoustic waveguide, as illustrated in Fig. 1. The resonator, of radius  $a$ , length  $L_R$  and with infinitely thin walls, is closed at the bottom end  $y = 0$ , and open (unflanged) at top  $y = L_R$ , with an associated acoustic radiation impedance  $Z_R$ . The beam has length  $L_B$  and its width is equivalent to the resonator diameter (2a). The central axis of the resonator is within the plane that crosses the beam width ( $z = 0$ ) and is located at a distance  $x_e$  along the beam length. Moreover, its open termination is located at a distance  $d$  below the bar.

### 2.1. Dynamics of the uncoupled bar

Several studies have shown that the sound radiated from a bar in mallet percussion instruments is dominated by the vibration of its vertical-bending modes, although torsional and lateral modes can also radiate and contribute to the bar sound [6,8]. However, in terms of bar-resonator interaction, it can be argued that non-vertical-bending modes (torsional/lateral) will not experience strong coupling. As for lateral modes, their main direction of vibration (plane  $x - z$ ) is perpendicular to the axis of the resonator, and therefore acoustic

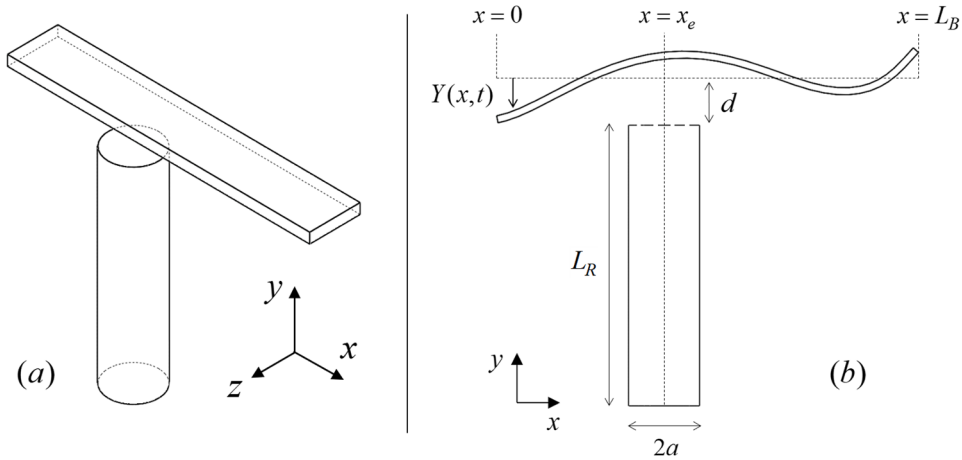


**Fig. 1.** Illustrative diagram of the considered model: (a) three-dimensional view; (b) cross-sectional view.

radiation towards the open end of the resonator is likely to be weak (or null). As for torsional modes, they have nodal lines along the length of the beam and hence, their acoustic radiation pattern will have pressure nulls in the plane  $z = 0$ , where the resonator is centered. Therefore, the spatial average of pressure felt in the open resonator termination is going to be null. We will therefore neglect the contribution of non-vertical-bending modes, and consider a one-dimensional beam, vibrating only in the vertical direction.

We consider the linear dynamics of a beam with length  $L_B$ , width  $2a$ , a variable thickness  $h(x)$  and free-free boundary conditions. Assuming proportional damping, the beam dynamics are described in a modal framework, given by the set of modal equations

$$m_n \ddot{\alpha}_n(t) + 2m_n \zeta_n \omega_n \dot{\alpha}_n(t) + m_n \omega_n^2 \alpha_n(t) = 0 \quad \text{for } n = 1, 2 \dots N \quad (1)$$

where  $m_n$ ,  $\zeta_n$ ,  $\omega_n$  and  $\alpha_n(t)$  are the modal masses, damping ratios, angular frequencies and amplitudes of the beam modes, respectively, and the beam vertical displacement  $Y(x, t)$  is given by the sum of the modal contributions

$$Y(x, t) = \sum_{n=1}^N \psi_n(x) \alpha_n(t) \quad (2)$$

where  $\psi_n(x)$  are the beam mode shapes. The beam modal parameters can be either calculated through various modeling approaches (Euler-Bernoulli, Timoshenko or 3-D beam theories [16]) or measured via experimental modal identification [17], as will be done in the experimental part of this work.

## 2.2. Acoustics of the uncoupled resonator

In a one-dimensional domain, the small oscillations of a fluid about a state of rest can be described by the linearized Euler equations [18]. From these, the acoustic wave equation can be derived in terms of some fluctuating variable of the fluid (pressure, particle displacement, density, etc.). In the field of acoustics, it is common practice to use the wave equation in terms of fluctuating pressure. However, in many practical applications, particularly in the field of vibro-acoustics, it is sometimes useful to model the acoustics in terms of another state variable. This is done in situations where the coupled vibro-acoustic system is not symmetric when using pressure as the acoustic variable [19]. Later in this section, it will become evident that, in this model, taking the particle displacement as the acoustic variable is the most practical approach. Therefore, the one-dimensional linear acoustic wave equation in terms of particle displacement  $w(y, t)$  is given by

$$\rho S \left( \frac{1}{c^2} \frac{\partial^2 w(y, t)}{\partial t^2} - \frac{\partial^2 w(y, t)}{\partial y^2} \right) = 0 \quad (3)$$

where  $\rho$  is the fluid density at rest,  $c$  is the speed of sound and  $S$  is the cross-sectional area of the pipe. The factor  $\rho S$ , even though less significant for the solutions of the uncoupled resonator (3), is important as later on, when the vibro-acoustic coupling is treated, forcing terms will be added to the right-hand-side of (3). At the closed end  $y = 0$ , the displacement is null and the boundary condition is written simply as

$$w(0, t) = 0 \quad (4)$$

while at the open (unflanged) end  $y = L_R$ , we impose a radiation impedance  $Z_R$  such that the pressure  $p(L_R, t)$  and acoustic particle velocity  $u(L_R, t)$  obey the following relation in the Laplace domain

$$Z_R(s) = \frac{p(L_R, s)}{u(L_R, s)} = \rho c (sX_R - s^2 R_R) \quad (5)$$

where  $s$  is the complex Laplace variable;  $R_R$  and  $X_R$  are associated to the acoustic resistance and reactance, respectively. Remembering Euler's continuity relation, we can write the fluctuating pressure in terms of particle displacement as

$$\rho \frac{\partial^2 w(y, t)}{\partial t^2} + \frac{\partial p(y, t)}{\partial y} = 0 \quad \Rightarrow \quad p(y, t) = -\rho \int \left( \frac{\partial^2 w(y, t)}{\partial t^2} \right) dy \quad (6)$$

Here, an arbitrary constant emerges from the integration, which without loss of generality we have taken to be zero [20]. Then, the boundary condition at the open-end  $y = L_R$  is written as

$$\frac{-\int_0^{L_R} w(y, s) dy}{w(L_R, s)} = c(X_R - sR_R) \quad (7)$$

Replacing the two boundary conditions (4) and (7) into the wave Eq. (3) eventually leads to the pipe's characteristic equation

$$\coth\left(\frac{sL_R}{c}\right) - s^2 R_R + sX_R = 0 \quad (8)$$

whose solutions  $s_r$  are the complex eigenvalues of the uncoupled resonator. While difficult to solve analytically for a generic case, the solutions can be found numerically to obtain the real and imaginary parts of the eigenvalue pairs  $s_r = a_r \pm jb_r$ , from which the undamped natural frequencies  $\underline{\omega}_r$  and damping ratios  $\underline{\zeta}_r$  of each acoustic mode  $r$  can be obtained

$$\underline{\omega}_r = \sqrt{a_r^2 + b_r^2} \quad ; \quad \underline{\zeta}_r = -a_r / \underline{\omega}_r \quad (9)$$

Additionally, the complex mode shapes  $\tilde{\phi}_r(y)$  are given as

$$\tilde{\phi}_r(y) = \sinh\left(\frac{s_r y}{c}\right) \quad (10)$$

### 2.2.1. Modal decomposition of the resonator acoustics

For non-ideal closed-open pipes, the orthogonality property does not strictly hold due to the effect of the acoustic reactance  $X_R$  and resistance  $R_R$ . When we account for the radiation damping ( $R_R > 0$ ) the eigenfrequencies and mode shapes become complex, which leads to a non-diagonal damping matrix  $C$  in the modal space and (formally) prevents a decoupling of the equations of motion. However, provided that modal damping is weak and the eigenfrequencies are well separated from each other, it can be shown [21] that the inter-modal damping coefficients  $\underline{\zeta}_{rm}$  are negligible, as well as their (first-order) effect on the mode shapes. Therefore, the equations of motion for the dissipative system can be assumed decoupled while maintaining the (real) mode shapes of the equivalent conservative system (assuming  $R_R = 0$ ), as demonstrated in detail in [21]. Under these simplifying, but reasonable, assumptions we can develop the particle displacement  $w(y, t)$  in terms of the (real) acoustic modes  $\phi_r(y)$  as

$$w(y, t) = \sum_{r=1}^R \phi_r(y) \gamma_r(t) , \quad \text{where } \phi_r(y) = \sin\left(\frac{\underline{\omega}_r}{c} y\right) \quad (11)$$

where  $\gamma_r(t)$  are the modal coordinates. Similarly, the effect of the added reactance  $X_R$  also leads to non-orthogonal mode shapes. For example, assuming the conservative mode shapes (11), the terms stemming from the Galerkin projection, in dimensionless form (with  $\bar{y} = y/L_R$ ), are given by

$$\int_0^1 \phi_n(\bar{y}) \phi_m(\bar{y}) d\bar{y} = \begin{cases} \frac{\sin(\alpha_n)}{2\alpha_n} + \frac{1}{2} & \text{for } m = n \\ \frac{\sin((\alpha_n - \alpha_m)/2)}{(\alpha_n - \alpha_m)} + \frac{\sin((\alpha_n + \alpha_m)/2)}{(\alpha_n + \alpha_m)} & \text{for } m \neq n \end{cases} \quad (12)$$

where  $\alpha_n$  (or equivalent for  $\alpha_m$ ) are auxiliary parameters given by

$$\alpha_n = \frac{\pi(2n-1)}{1 + 0.6133(a/L_R)} \quad (13)$$

where, to emphasize the role of the pipe aspect ratio  $a/L$ , here we assume the typical low-frequency ( $ka < 1$ ) approximation for an unflanged pipe  $X_R = 0.6133a/c$  [22]. However, it can be shown that for pipes that are not unreasonably wide ( $a/L_R < 0.1$ ), the contributions of off-diagonal terms are small and the following orthogonal approximation is suitable

$$\int_0^L \phi_n(y) \phi_m(y) dy \approx \begin{cases} \frac{L_R + \Delta L}{2} & \text{for } m = n \\ 0 & \text{for } m \neq n \end{cases} \quad (14)$$

where  $\Delta L$  is the length correction term ( $\Delta L = X_{RC}$ ). It is worth mentioning that in commercial instruments, resonator pipes with large aspect ratios  $a/L_R > 0.1$  are rare, and occur only in the highest register of some instruments (see [23] for example). For simplicity, here we make use of the orthogonal approximation (14) and eventually reach the set of linearly independent modal equations describing the resonator acoustics

$$\underline{m}_r \ddot{\gamma}_r(t) + 2\zeta_r \underline{m}_r \underline{\omega}_r \dot{\gamma}_r(t) + \underline{m}_r \underline{\omega}_r^2 \gamma_r(t) = 0 \quad \text{for } r = 1, 2 \dots R \quad (15)$$

where the inertial modal coefficients  $\underline{m}_r$  are given by

$$\underline{m}_r \simeq \rho S \left( \frac{L_R + \Delta L}{2} \right) \quad (16)$$

Nevertheless, nothing formally prevents the use of expression (12), which would lead to a set of weakly coupled oscillators describing the resonator acoustics. Note, however, that all expressions presented in this section are based on a low-frequency approximation of the radiation impedance (valid for  $ka < 1$ ). Therefore, higher order acoustic modes with (dimensionless) natural frequencies  $k_r a > 1$ , may require a more precise account of the radiation impedance. As an example, in a cylindrical closed-open pipe with aspect ratio  $a/L_R = 0.1$ , only the first three acoustic modes obey  $k_r a < 1$ .

### 2.2.2. Radiation impedance of an open pipe with a partial obstruction

A first approximation of the acoustic radiation impedance of an open (unflanged) pipe is given by the commonly used low-frequency approximation [24]

$$\bar{Z}_R(ka) = \frac{1}{4}(ka)^2 + j0.6133(ka) \quad \text{for } ka < 1 \quad (17)$$

where  $ka$  is the dimensionless frequency,  $k = \omega/c$ , and  $\bar{Z}_R$  is normalized by the characteristic impedance  $\rho c/S$ . However, the presence of a solid object (in our case the bar) near the open-end will modify radiation impedance of the pipe. This phenomenon is commonly known to builders and often results in a noticeable decrease of its natural frequencies.

In a recent work by the authors [15], an attempt was made to model this behavior whereby the presence of the bar was approximated by a rigid circular disk of the same radius as the cylindrical pipe, located at a distance  $d$  above the open-end. A 2-D axisymmetric finite element model was used to numerically calculate the radiation impedance of the partially obstructed open-end, for various values of the dimensionless disk distance  $d/a$ . It was proposed that the (normalized) radiation impedance, with the presence of a rigid disk, can be approximated in the low-frequency range ( $ka < 1$ ) by

$$\bar{Z}_r(ka, d/a) = \frac{1}{4}(ka)^2 + j\left(\eta \frac{a}{d} + 1\right)0.6133(ka) \quad (18)$$

where the coefficient  $\eta$  was calculated via a linear fitting on the FE numerical results, yielding  $\eta \approx 0.32$ . Nevertheless, the value of  $\eta$  could also be fitted to measured results using real bars. Note that, as expected, when  $d \rightarrow 0$ , the reactance tends infinity as that of a closed pipe, and when  $d \rightarrow \infty$ , the reactance tends to the low-frequency approximation of an (unflanged) open pipe (17). In the experimental part of this work, this impedance model will be confronted by experimental results to assess its range of validity and find the most appropriate value for the coefficient  $\eta$ .

### 2.3. Vibro-acoustic coupling

The most challenging aspect in modeling the dynamic interaction between a vibrating beam and an acoustic resonator is associated with the three-dimensional effects of the acoustic radiation that couple the two mechanical-acoustical elements. Here, we simplify the problem by assuming that only a particular region in the beam surface will have a meaningful vibro-acoustic interaction with the resonator. Namely, we consider the circular area on the beam that is located directly above the open-end of the resonator, as illustrated in Fig. 2. Although a rather crude geometric simplification, it may nevertheless be a reasonable initial approximation to what happens in real instruments as, naturally, this region of the beam will be dominant in the vibro-acoustic coupling.

Then, the vibro-acoustic coupling will be defined by the interaction between the motion of this circular area on the beam and the acoustics of the adjacent circular surface, i.e. the open-end of the resonator. Since the two surfaces are not directly linked, we model their interaction in terms of mutual excitations. On this point, we remind the reader of the principle of vibro-acoustical reciprocity [25, 26], which in its simplest form states that: the transfer function between the motion of a structure  $\dot{Y}_j$  (acceleration) at point  $j$  and a response pressure  $p_i$  in the acoustic domain at point  $i$ , is equivalent to the transfer function between an acoustic source  $\dot{q}_i$  (volume acceleration) at point  $i$  and the resulting force load on the structure at point  $j$ , that is

$$\frac{p_i}{\dot{Y}_j} = \frac{f_j}{\dot{q}_i} \quad (19)$$

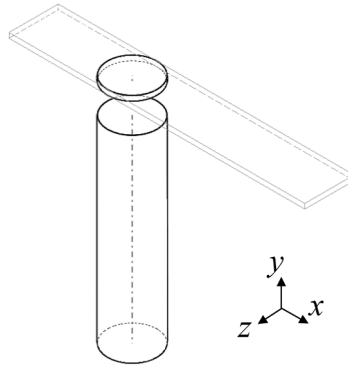


**Fig. 2.** Illustration of the portion of the beam considered in the vibro-acoustic interaction.

This principle can also be re-arranged in the form of a dimensionless transfer function  $H$ , which in our problem can be written, in the frequency domain, as

$$H(\omega) = \frac{F_a(x_e, \omega)}{p(L_R, \omega)S} = \frac{\dot{Q}_b(L_R, \omega)}{\ddot{Y}(x_e, \omega)} \quad (20)$$

where  $\dot{Q}_b(L_R, \omega)$  is an acoustic volume acceleration induced on the resonator open-end by the beam-disk motion and, similarly,  $F_a(x_e, \omega)$  is the net force induced on the beam-disk by the acoustic radiation from the open-end of the resonator. Notice that in this formulation, all quantities are spatially averaged over the surface area  $S$ , and concentrated on a single point located at  $x = x_e$ . The transfer function can be re-written in terms of acoustic particle displacement as

$$H(\omega) = \frac{F_a(x_e, \omega)}{-\rho S \int_0^{L_R} \ddot{w}(y, \omega) dy} = \frac{\dot{Q}_b(L_R, \omega)}{\ddot{Y}(x_e, \omega)} \quad (21)$$

In a recent work [14,15] this transfer function was numerically calculated in the frequency domain, via a 2-D axisymmetric finite element model considering the interaction between two parallel circular surfaces of the same radius  $a$ , for various separation distances  $d/a$ . It was found that, in the low-frequency range ( $ka < 1$ ), the transfer function  $H(ka, d/a)$  can be approximated by a simple constant gain filter, dependent solely on the dimensionless distance  $d/a$ . For more details on the derivation of this approximate transfer function, as well as its numerical validation against a vibro-acoustic FE model, the reader is referred to the author's previous work [14, 15]. As illustrated in Fig. 3, the FE numerical results were fitted to a polynomial function of the following form

$$H(d/a) = \left( 1 + \sum_{p=1}^P \delta_p \left( \frac{d}{a} \right)^p \right)^{-1} \quad (22)$$

considering various orders  $P$ . For example, the best fitted coefficients in a 5th-order polynomial were  $\delta_p = [2.78, -1.03, 3.34, -1.15, 0.13]$ . Notice that, when  $d \rightarrow 0 \Rightarrow H \rightarrow 1$  and when  $d \rightarrow \infty \Rightarrow H \rightarrow 0$ , as expected. Finally, with the knowledge of  $H(d/a)$ , the force  $F_a(x_e, t)$  and the acoustic excitation  $\dot{Q}_b(L_R, t)$  can be used as forcing terms in the equations of the beam (1) and of the resonator (15), respectively.

It is worth mentioning that a recent publication [27] presents an analytical formulation for the calculation of the self and mutual

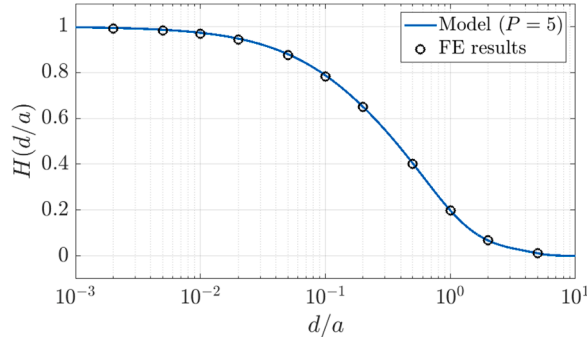


**Fig. 3.** Comparison between the low frequency approximation of the function  $H(d/a)$  calculated by the FE model and the polynomial approximation of order  $P = 5$ .

radiation impedances of spheroids. Although set in a slightly different framework, it could potentially be used to model the transfer function  $H(ka, d/a)$  analytically.

#### 2.4. Derivation of the coupled system

Given the definitions of the vibro-acoustic transfer function in (21) and (22), the force load on the beam-disk induced by the resonator is then given by

$$F_a(x, t) = -\delta(x - x_e)\rho SH(d/a) \sum_{r=1}^R \ddot{\gamma}_r(t) \varphi_r(L_R) \quad (23)$$

where the auxiliary functions  $\varphi_r(y)$  (associated with the resonator mode shapes in terms of pressure) are given by

$$\varphi_r(y) = \int \phi_r(y) dy = -\left(\frac{c}{\omega_r}\right) \cos\left(\frac{\omega_r}{c}y\right) \quad (24)$$

Subsequently, projection onto the beam modal basis  $\psi_n(x)$  will yield the modal forces  $F_n(t)$  applied on each beam mode

$$F_n(t) = \rho SH(d/a) \sum_{r=1}^R \varphi_r(L_R) \ddot{\gamma}_r(t) \int_0^{L_B} (\delta(x - x_e) \psi_n(x)) dx \quad (25)$$

for  $n = 1, 2 \dots N$ . Finally, the beam modal equations are given by

$$m_n \ddot{\alpha}_n(t) + 2m_n \omega_n \zeta_n \dot{\alpha}_n(t) + m_n \omega_n^2 \alpha_n(t) = \rho SH(d/a) \psi_n(x_e) \sum_{r=1}^R \varphi_r(L_R) \ddot{\gamma}_r(t) \quad (26)$$

for  $n = 1, 2 \dots N$ . Similarly, the volume acceleration induced on the resonator by the beam-disk motion is given by

$$\dot{Q}_b(L_R, t) = SH(d/a) \ddot{Y}(x_e, t) \quad (27)$$

Using (27) as a forcing term in the (inhomogeneous) wave equation and after the appropriate Galerkin projection unto the acoustic modal basis, the resonator modal equations are given by

$$\underline{m}_r \ddot{\gamma}_r(t) + 2\underline{m}_r \underline{\omega}_r \zeta_r \dot{\gamma}_r(t) + \underline{m}_r \underline{\omega}_r^2 \gamma_r(t) = -\rho SH(d/a) \varphi_r(L_R) \sum_{n=1}^N \psi_n(x_e) \ddot{\alpha}_n(t) \quad (28)$$

for  $r = 1, 2 \dots R$ . The final coupled system is then described by a series of  $N$  (mechanical) oscillators inertially coupled to  $R$  (acoustic) oscillators

$$\begin{bmatrix} \mathbf{M}_B & \Pi \\ \Pi^T & \mathbf{M}_R \end{bmatrix} \begin{Bmatrix} \ddot{\alpha} \\ \ddot{\gamma} \end{Bmatrix} + \begin{bmatrix} \mathbf{C}_B & 0 \\ 0 & \mathbf{C}_R \end{bmatrix} \begin{Bmatrix} \dot{\alpha} \\ \dot{\gamma} \end{Bmatrix} + \begin{bmatrix} \mathbf{K}_B & 0 \\ 0 & \mathbf{K}_R \end{bmatrix} \begin{Bmatrix} \alpha \\ \gamma \end{Bmatrix} = \begin{Bmatrix} \mathbf{0} \\ \mathbf{0} \end{Bmatrix} \quad (29)$$

where the vectors  $\alpha$  and  $\gamma$  contain the modal coordinates of the bar and resonator modes, respectively. The modal sub-matrices  $\mathbf{M}_B$ ,  $\mathbf{C}_B$ ,  $\mathbf{K}_B$ ,  $\mathbf{M}_R$ ,  $\mathbf{C}_R$  and  $\mathbf{K}_R$  are diagonal and define the modal parameters of the beam and resonator, i.e.

$$\begin{aligned} \text{diag}(\mathbf{M}_B) &= m_n & \text{diag}(\mathbf{C}_B) &= 2\zeta_n m_n \omega_n & \text{diag}(\mathbf{K}_B) &= m_n \omega_n^2 & ; \\ \text{diag}(\mathbf{M}_R) &= \underline{m}_r & \text{diag}(\mathbf{C}_R) &= 2\underline{\zeta}_r \underline{m}_r \underline{\omega}_r & \text{diag}(\mathbf{K}_R) &= \underline{m}_r \underline{\omega}_r^2 & ; \end{aligned} \quad (30)$$

while the inertial coupling matrix is given by

$$\Pi = \rho SH(d/a) \begin{bmatrix} \varphi_1(L_R) \psi_1(x_e) & \varphi_2(L_R) \psi_1(x_e) & \cdots & \varphi_R(L_R) \psi_1(x_e) \\ \varphi_1(L_R) \psi_2(x_e) & \varphi_2(L_R) \psi_2(x_e) & & \vdots \\ \vdots & & & \ddots \\ \varphi_1(L_R) \psi_N(x_e) & & & \varphi_R(L_R) \psi_N(x_e) \end{bmatrix} \quad (31)$$

It is interesting to note that the coupled system derived above is analogous to that of a string coupled to a soundboard (as occurs for example in pianos or guitars), for which the reader can find a detailed analysis in [28], for example.

#### 2.5. Energy balance

The coupled system (29) can easily be analyzed from an energetic standpoint. The kinetic and potential modal energies,  $T_n(t)$  and  $U_n(t)$ , contained in each beam mode are given

$$T_n(t) = \frac{m_n}{2} \dot{\alpha}_n^2(t) \quad ; \quad U_n(t) = \frac{m_n \omega_n^2}{2} \alpha_n^2(t) \quad (32)$$

Similarly, the acoustic kinetic and potential modal energies in each resonator mode,  $\underline{T}_r(t)$  and  $\underline{U}_r(t)$ , are given by

$$\underline{T}_r(t) = \frac{m_r}{2} \dot{\gamma}_r^2(t) \quad ; \quad \underline{U}_r(t) = \frac{m_r \omega_r^2}{2} \gamma_r^2(t) \quad (33)$$

The accumulated amount of energy dissipated by each beam mode, via internal losses, is given by

$$D_n(t) = 2\zeta_n m_n \omega_n \int_0^t \dot{\alpha}_n^2(\tau) d\tau \quad (34)$$

while the amount of energy dissipated by each resonator mode, through acoustic radiation, is given by

$$\underline{D}_r(t) = 2\zeta_r m_r \omega_r \int_0^t \dot{\gamma}_r^2(\tau) d\tau \quad (35)$$

The energy conserved in a given coupled-pair  $nr$  (single bar mode coupled to a single resonator mode) is given by

$$E_{C,nr}(t) = U_n(t) + T_n(t) + \underline{U}_r(t) + \underline{T}_r(t) \quad (36)$$

Finally, by energy conservation and under free vibration conditions, the following relation expressing the total energy in the system holds

$$E_T = \sum_{n=1}^N [U_n(t) + T_n(t) + D_n(t)] + \sum_{r=1}^R [\underline{U}_r(t) + \underline{T}_r(t) + \underline{D}_r(t)] = \text{constant} \quad (37)$$

It is worthwhile noting that in the current model, some mechanisms of energy dissipation, usually present in realistic scenarios, have been neglected (e.g. the energy dissipated by the bar through acoustic radiation or via coupling the its supporting elastic strings, as well as visco-thermal losses in the resonator).

### 3. Illustrative example of single mode coupling

In realistic scenarios, the natural frequencies of a musical bar will be well-separated and hence, each mode of the beam will typically experience significant coupling effects only to one mode of the resonator. In this context, to illustrate the nature of the coupled dynamics, we now consider a system composed of a single generic beam mode ( $n$ ) and a single generic resonator mode ( $r$ ), described by

$$\begin{bmatrix} m_n & \Pi_{nr} \\ \Pi_{nr} & \underline{m}_r \end{bmatrix} \begin{Bmatrix} \ddot{\alpha}_n \\ \dot{\gamma}_r \end{Bmatrix} + \begin{bmatrix} 2m_n \omega_n \zeta_n & 0 \\ 0 & 2\underline{m}_r \underline{\omega}_r \zeta_r \end{bmatrix} \begin{Bmatrix} \dot{\alpha}_n \\ \dot{\gamma}_r \end{Bmatrix} + \begin{bmatrix} m_n \omega_n^2 & 0 \\ 0 & \underline{m}_r \underline{\omega}_r^2 \end{bmatrix} \begin{Bmatrix} \alpha_n \\ \gamma_r \end{Bmatrix} = \begin{Bmatrix} 0 \\ 0 \end{Bmatrix} \quad (38)$$

where the inertial coupling term is

$$\Pi_{nr} = \rho S H(d/a) \varphi_r(L_R) \psi_n(x_e) \quad (39)$$

The dynamics of the coupled system will vary qualitatively depending on three dimensionless parameters: the tuning ratio  $\underline{\omega}_r / \omega_n$ , the dissipation ratio  $\zeta_r / \zeta_n$  and a coupling “strength” coefficient  $\sigma_{nr}$  (related to  $\Pi_{nr}$ , defined in the subsequent section). In the following sub-sections, we present some example results from eigenvalue analysis and time-domain integrations to illustrate the behavior of the system and the role of each dimensionless parameter.

#### 3.1. Coupled mode analysis

The two (conjugate) pairs of eigenvalues  $\lambda_{1,2} = A_{1,2} \pm jB_{1,2}$  of the coupled system (38) are given by the roots of the characteristic equation

$$(\omega_n^2 + 2\zeta_n \omega_n \lambda + \lambda^2)(\underline{\omega}_r^2 + 2\zeta_r \underline{\omega}_r \lambda + \lambda^2) = \lambda^4 \sigma_{nr}^2 \quad (40)$$

where the dimensionless inertial coupling coefficient  $\sigma_{nr}$  is given explicitly by

$$\sigma_{nr} = \frac{\rho S H(d/a) \varphi_r(L_R) \psi_n(x_e)}{\sqrt{m_n \underline{m}_r}} \quad (41)$$

and the frequencies  $\Omega_{1,2}$  and damping ratios  $\Delta_{1,2}$  of its coupled modes are retrieved from

$$\Omega_{1,2} = \sqrt{A_{1,2}^2 + B_{1,2}^2} \quad ; \quad \Delta_{1,2} = -A_{1,2} / \Omega_{1,2} \quad (42)$$

As in most systems of coupled linear oscillators, strong coupling effects occur when their natural frequencies are comparable  $\underline{\omega}_r / \omega_n \approx 1$ . To illustrate, Fig. 4 shows the evolution of the frequencies  $\Omega_{1,2}$  and damping ratios  $\Delta_{1,2}$  of the coupled modes, as a function of the tuning ratio  $\underline{\omega}_r / \omega_n$ , for two different values of the coupling “strength”  $\sigma_{nr}$ . Here, the dissipation ratio was fixed at  $\underline{\zeta}_r / \zeta_n = 10$ .

We notice that the eigenvalue pairs  $\lambda_{1,2}$  cross in the vicinity of  $\underline{\omega}_r / \omega_n = 1$ . Moreover, for fixed damping ratios, they can cross in their imaginary part ( $\Omega_{1,2}$ ) or their real part ( $\Delta_{1,2}$ ) depending on the strength of the coupling  $\sigma_{nr}$ . For weak coupling ( $\sigma_{nr} = 0.0015$ ), the two (coupled) modes will vibrate at the same frequency but with distinct damping. For strong coupling ( $\sigma_{nr} = 0.005$ ), the two modes vibrate at distinct frequencies but with the same damping rate, approximately equal to  $\Delta_{1,2} = (\underline{\zeta}_r + \zeta_n)/2$ . The interested reader is referred to the analysis presented in [28], where a similar system is studied in detail. There, the authors derive an approximate relation for the change in behavior as  $\sigma_{nr}^2 \simeq (\underline{\zeta}_r + \zeta_n)^2$ .

In the context of mallet percussion instruments, the latter result suggests that if the resonator mode has a larger damping ratio than the bar mode  $\underline{\zeta}_r > \zeta_n$  (which is the most often scenario), coupling will result in a relative increase of the system’s damping rate, i.e. a decrease of its decay time, as commonly reported in experimental observations. Naturally, this decrease in decay time will be associated with the energy that is more efficiently dissipated through the resonator (as acoustic radiation), instead of through internal losses in the bar. This explains the commonly seen compromise between an increase in sound radiation and a decrease in decay time. Effectively then, a resonator with a large damping ratio  $\underline{\zeta}_r$  will tend to increase this effect. This underlines the importance of the dissipation ratio  $\underline{\zeta}_r / \zeta_n$ , which should be taken as a design criterion in the optimization of these instruments.

On the other hand, when the resonator damping is smaller than bar damping  $\underline{\zeta}_r < \zeta_n$ , results suggest that decay time will be increased. Although an unlikely scenario in instruments with metallic bars (which generally have very low damping ratios), these cases might be found in instruments with wooden bars, like marimbas or xylophones, where damping ratios  $\underline{\zeta}_r$  and  $\zeta_n$  tend to fall within the same order of magnitude. To illustrate, Fig. 5 shows the evolution of damping ratios of the coupled modes  $\Delta_{1,2}$ , as a function of the dissipation ratio  $\underline{\zeta}_r / \zeta_n$ , for a perfectly tuned case ( $\underline{\omega}_r / \omega_n = 1$ ).

Note that when  $\underline{\zeta}_r / \zeta_n < 1$ , the damping of the coupled modes remains in the bottom-left quadrant (i.e. increase in decay time) while for  $\underline{\zeta}_r / \zeta_n > 1$ , the damping of the coupled modes stays in the top-right quadrant (i.e. decrease in decay time). Moreover, larger dissipation ratios  $\underline{\zeta}_r / \zeta_n$  will have a decoupling effect, where the two “coupled” modes tend to those of the uncoupled oscillators.

Another interesting aspect to note in this single-mode analysis is the parameters affecting the coupling coefficient  $\sigma_{nr}$  (41). Aside from the obvious influence of the vibro-acoustic function  $H(d/a)$ , we also note that the coupling is dependent on the bar mode shape at the location where the resonator is placed  $\psi_n(x_e)$ . This means that, if the resonator is directly below a nodal line of the bar mode, the two oscillators will be decoupled. This seems physically plausible as the acoustic radiation patterns of a bar mode will generally show pressure nulls at nodal locations, as illustrated in Fig. 6. In these cases, the spatially averaged pressure at the resonator open surface

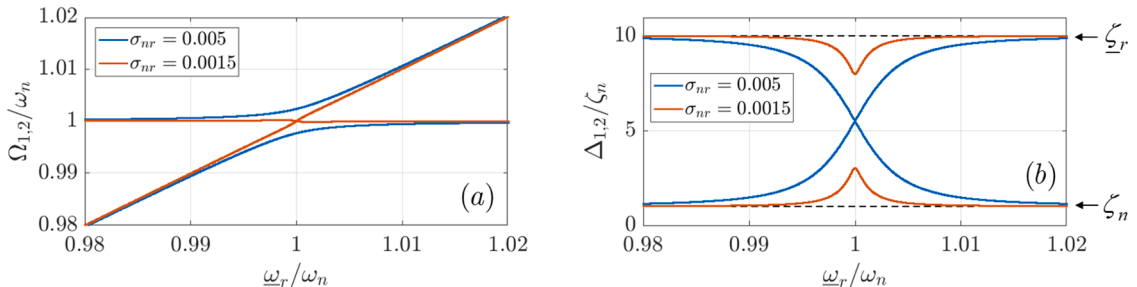


**Fig. 4.** Evolution of (a) frequencies and (b) damping ratios of the coupled system as a function of the tuning ratio  $\underline{\omega}_r / \omega_n$ , for two values of the coupling coefficient  $\sigma_{nr}$ . Here the dissipation ratio is set to  $\underline{\zeta}_r / \zeta_n = 10$ .

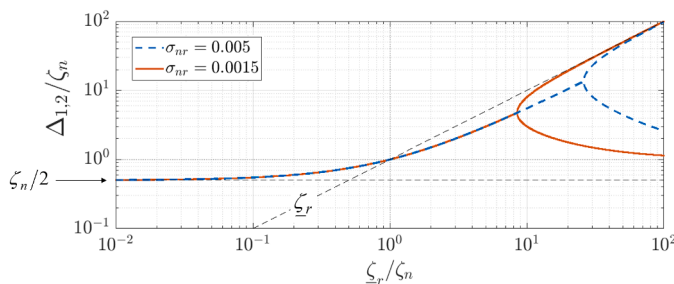


**Fig. 5.** Evolution of damping ratios of the coupled modes as a function of the dissipation ratio  $\underline{\zeta}_r / \zeta_n$ , for two values of the coupling coefficient  $\sigma_{nr}$ , in a perfectly tuned case  $\underline{\omega}_r / \omega_n = 1$ .

will be zero. This underlines the importance of the resonator placement along the bar length  $x_e$  as well as the modal shape of the bar at the coupling point  $\psi_n(x_e)$ .

Similarly, the coupling strength  $\sigma_{nr}$  will depend on the acoustic mode shapes of the resonator (in terms of pressure) at the termination surface  $\varphi_r(L_R)$ . This occurs because the reactive term in the acoustic radiation impedance (17) leads to mode shapes without a pressure node at the open termination, contrary to the case of *ideal* closed-open pipes. When considering cylindrical resonators, the value of  $\varphi_r(L_R)$  is imposed. However, in the advent of designing optimized resonators, as in [10], this parameter could eventually be considered in the optimization process.

### 3.2. Illustrative time-domain simulations

To illustrate the behavior of a single mode coupled system more clearly, we now show some time-domain integrations. We firstly consider a system with the following parameters:  $\zeta_n = 3 \times 10^{-4}$ ,  $m_n = 0.2$  kg,  $\omega_n = 1100$  rad · s<sup>-1</sup> and  $\zeta_r/\zeta_n = 5$ ,  $m_r/m_n = 0.0025$ ,  $\sigma_{nr} = 0.002$ . This parameter configuration corresponds approximately to what would be found in the low-register of a typical vibraphone. Initial conditions are taken with the resonator mode at rest  $\gamma_r(0) = \dot{\gamma}_r(0) = 0$ , while the bar mode is given an initial velocity, i.e.  $\alpha_n(0) = 0$  and  $\dot{\alpha}(0) = 1$ . Fig. 7 shows the energetic distribution in the system as a function of time, for both tuned  $\omega_r/\omega_n = 1$  and untuned  $\omega_r/\omega_n = 0.99$  configurations.

The responses shown in Fig. 7 illustrate well the behavior commonly observed in experiments, whereby a tuned configuration leads to a stronger excitation of the resonator mode but also to a significant decrease in the bar decay time. Results illustrate that in a tuned scenario, most of the energy initially provided to the system will be dissipated through acoustic radiation ( $D_r(t)$ ) rather than internal losses in the beam mode ( $D_n(t)$ ), as is for the untuned case. Effectively, this means that the role of the resonator is to convert the vibrational energy of the bar into audible sound. The interested reader can find remarkably similar results in the recent work by Rucz *et al.* [13], where a three-dimensional FE modeling approach was used.

In the context of free vibrations, a useful indicator of the role of the resonator can be given by a “modal radiation efficiency”  $\kappa_{nr}$ , representing the percentage of energy in the coupled-pair  $nr$  that is dissipated through acoustic radiation by the resonator mode  $r$ , that is

$$\kappa_{nr} = \frac{D_r(t \rightarrow \infty)}{E_{T,nr}} \times 100 \% \quad (43)$$

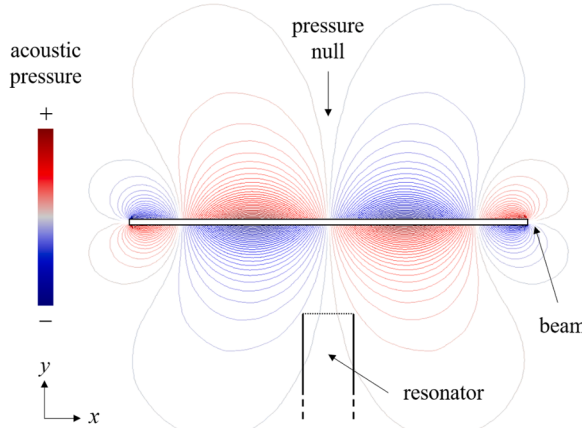


**Fig. 6.** Cross-sectional view (central  $x - z$  plane) of the acoustic radiation pattern of the second bending mode  $\psi_2(x)$  of a uniform bar.

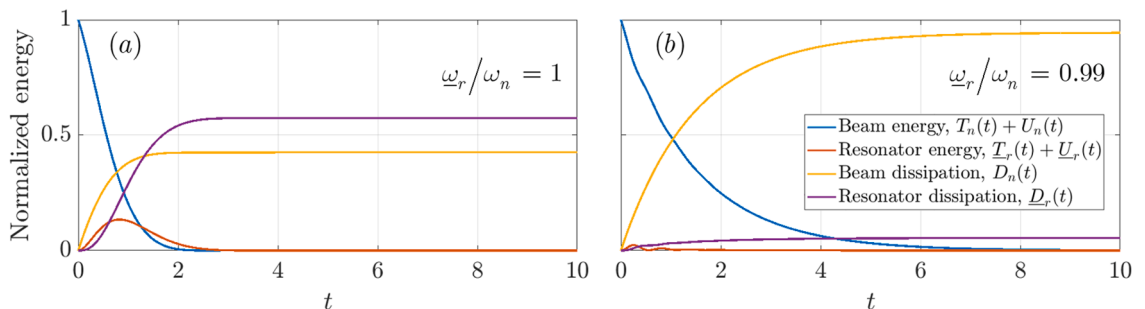


**Fig. 7.** Distribution of the energy in the coupled system for the (a) tuned case and (b) untuned case. All values are normalized by the initial energy, i.e.  $E_T = T_n(0) = m_n/2$ .

where  $E_{T,nr}$  is the total energy (constant) in the coupled-pair, given explicitly by  $E_{T,nr} = U_n(t) + T_n(t) + U_r(t) + T_r(t) + D_n(t) + D_r(t)$ .

Additionally, we define the decay time of the coupled-pair,  $T_{30,nr}$ , as the time it takes for its energy to decay by 30 dB (i.e. to 0.1% of its initial energy),

$$T_{30,nr} \Rightarrow \frac{E_{C,nr}(T_{30,nr})}{E_{C,nr}(0)} = 0.001 \quad (44)$$

To assess the variance of the two indicators,  $\kappa_{nr}$  and  $T_{30,nr}$ , several time-domain integrations were performed for multiple configurations, varying the three main dimensionless parameters:  $\underline{\omega}_r/\omega_n$ ,  $\underline{\zeta}_r/\zeta_n$  and  $\sigma_{nr}$ . Results are shown in Fig. 8.

The results in Fig. 8 illustrate that the typical compromise between increased sound radiation and a decrease in decay time is particular to configurations where the resonator damping is larger than the bar damping,  $\underline{\zeta}_r/\zeta_n > 1$ . For cases where  $\underline{\zeta}_r/\zeta_n < 1$ , a scenario possibly found in instruments with wooden bars [29], model results show that the coupled system will both increase sound radiation as well as increase the decay time  $T_{30,nr}$ . In the experimental part of this work, we will confront modeling results with experimental ones to validate and clarify this (perhaps counterintuitive) behavior. Notice that, the radiation efficiency is significantly lower for the configuration with  $\zeta_n = 0.3\%$ . This is not surprising since bars with large damping will inevitably dissipate large amounts of energy through internal losses, with or without the presence of the resonator.

#### 4. An optimized instrument with multi-modal coupling

In this section we aim to illustrate the capacity of the model to simulate systems with multi-modal coupling and how this could be used in the development of new instruments, where several resonator modes are tuned with several bar modes.

We consider an aluminum bar whose undercut leads to a frequency ratio of the first four vertical-bending modes of (1:4:10:16). Its fundamental frequency is set to  $\omega_1/2\pi = 175$  Hz. The characteristics of this (virtual) bar are based on optimized bars built in [6] and approximate what would be found in the lowest register of a typical vibraphone. The considered modal parameters are shown in Table 1 and Fig. 9-(a) shows the undercut profile of the bar  $h(x)$  and its mode shapes  $\psi_n(x)$ . Then, we consider two types of resonators: (1) a common cylindrical pipe, with the tuning ratio (1:3:5:7, etc.); and (2) an optimized axisymmetric resonator (with variable radius  $R(y)$ ), whose first five acoustic modes are tuned as (1:4:5.3:7.7:10). The latter is inspired by the work of Henrique et al. [9,10], and was

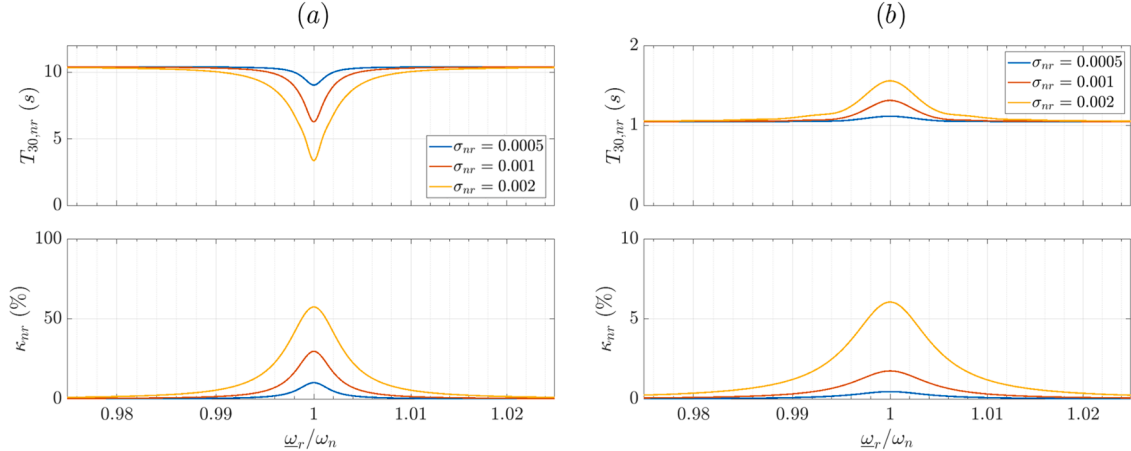


**Fig. 8.** Evolution of the decay time  $T_{30,nr}$  and the modal radiation ‘efficiency’  $\kappa_{nr}$  as a function of the tuning ratio  $\underline{\omega}_r/\omega_n$ , for various coupling ‘strengths’  $\sigma_{nr}$  in: (a) the case where  $\underline{\zeta}_r/\zeta_n > 1$  and (b) shows the case  $\underline{\zeta}_r/\zeta_n < 1$ . For case (a) damping values were fixed at  $\zeta_n = 0.03\%$  and  $\underline{\zeta}_r/\zeta_n = 5$ , while for case (b) these are  $\zeta_n = 0.3\%$  and  $\underline{\zeta}_r/\zeta_n = 0.5$ .

**Table 1**  
Considered modal parameters for the aluminum bar and the two acoustic resonators.

$n,r$	Bar			Resonator (cylindrical)			Resonator (optimized)		
	$\omega_n/2\pi$ (Hz)	$\zeta_n$ (%)	$m_n$ (kg)	$\underline{\omega}_r/2\pi$ (Hz)	$\underline{\zeta}_r$ (%)	$m_r$ (g)	$\omega_r/2\pi$ (Hz)	$\zeta_r$ (%)	$m_r$ (g)
1	175	0.03	0.058	175	0.25	0.57	175	0.25	0.46
2	700	0.03	0.086	525	0.31	0.57	700	0.42	0.47
3	1750	0.03	0.074	875	0.49	0.57	926	0.75	0.33
4	2800	0.03	0.073	1225	0.65	0.57	1352	0.85	0.43
5	–	–	–	1575	0.79	0.57	1750	1.14	0.43
6	–	–	–	1925	0.89	0.57	2145	1.31	0.40
7	–	–	–	2275	0.96	0.57	2538	1.47	0.39
8	–	–	–	2625	1.00	0.57	2927	1.61	0.40

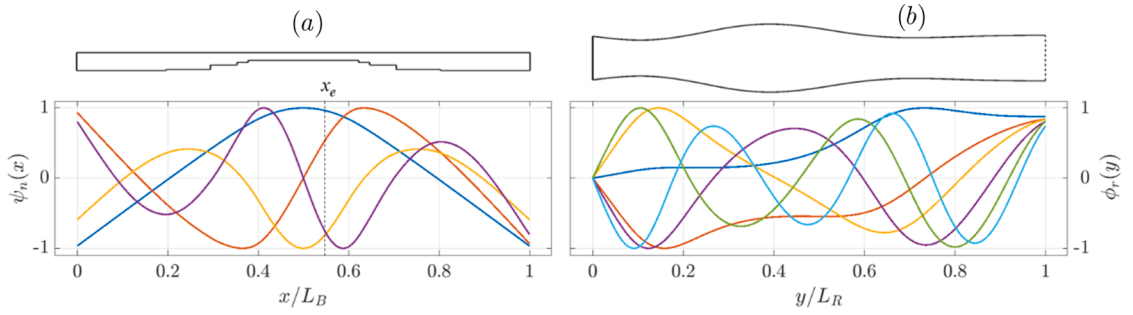


**Fig. 9.** Profile of (a) the optimized bar and (b) optimized resonator, as well as the resulting bar mode shapes  $\psi_n(x)$  and acoustic mode shapes  $\phi_r(y)$  (in terms of particle displacement).

optimized such that the first, second and fifth modes are tuned to the first three bar frequencies. Fig. 9-(b) shows the profile of the optimized resonator as well as its first six modes shapes  $\phi_r(y)$ . The fundamental mode of both resonators is tuned to the frequency of the first bar mode. The modal parameters considered are shown in Table 1. For equal comparison, the damping ratio of the first acoustic mode was fixed at  $\underline{\zeta}_1 = 0.25\%$  for both resonators. If only radiation losses are considered, these values would give  $\underline{\zeta}_1 = 0.11\%$  and  $\underline{\zeta}_1 = 0.13\%$  for the cylindrical and optimized resonators, respectively. However, the effect of visco-thermal losses would lead to larger damping ratios, at least for the lowest acoustic modes [30]. Similarly, the modal mass of the optimized resonator was fixed at  $\underline{m}_r = 0.46$  g, such that both configurations have the same dimensionless coupling strength  $\sigma_{11} = 0.0025$  (the actual value calculated was of  $\underline{m}_r = 0.40$  g). All other parameters were estimated through finite-element methods.

The bar-resonator distance was fixed at  $d/a = 0.5$  and the resonators are placed slightly off-centered  $x_e/L_B = 0.55$ , to avoid nodal lines of the bar modes (see Fig. 9-(a)). Two simulations were carried out with each of the resonators, by solving the system of equations defined in (29). To emulate the impact of a mallet, a gaussian pulse was used to excite the bar at its tip  $x = L_B$ . Effectively, a forcing term was added on the right-hand-side of (29), describing the projection of the gaussian pulse force onto each of the beam modes. The width of the gaussian pulse was chosen short enough such that its power spectrum is constant up to the frequency of the highest considered bar mode ( $\sim 3$  kHz).

Fig. 10 shows spectrograms of the signals obtained in the two temporal integrations, using both the cylindrical and optimized resonators. The resonator responses are shown in terms of the pressure at the end termination  $p(L_R, t)$ , while the bar responses are described by the acceleration of its tip  $\ddot{Y}(L_R, t)$ .

In regards to the 1st bar mode (175 Hz), we note that bar and resonator responses are the same in both configurations. This is expected since all three dimensionless parameters in this coupled-pair ( $\underline{\omega}_1/\omega_1$ ,  $\underline{\zeta}_1/\zeta_1$  and  $\sigma_{11}$ ) have the same value. As for the 2nd and

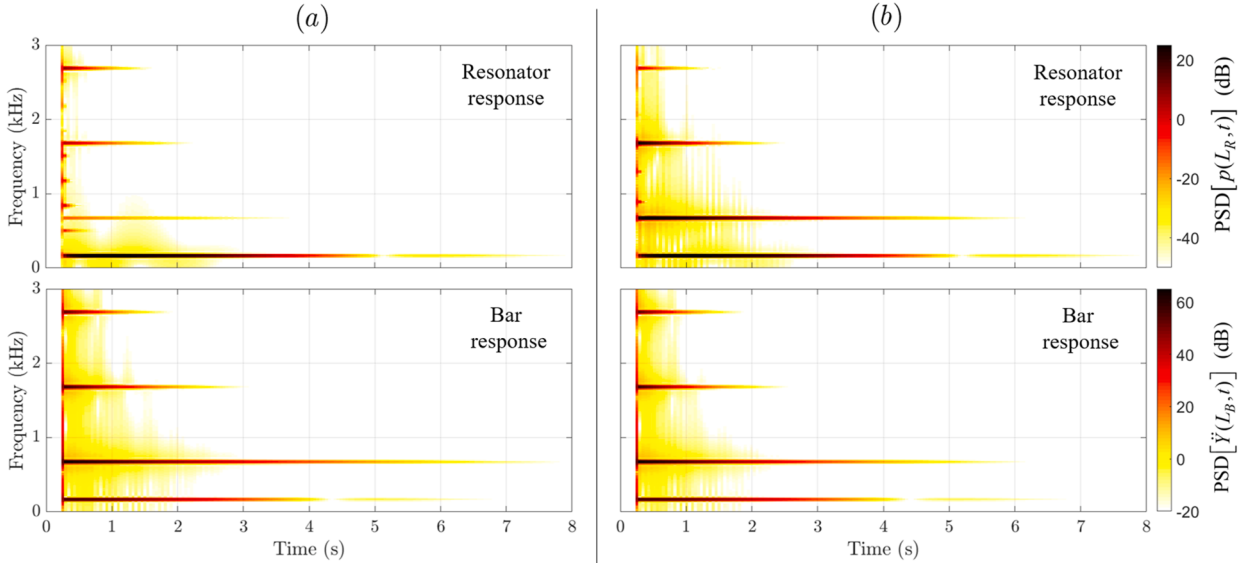


**Fig. 10.** Spectrograms of signals from the simulations using (a) the cylindrical resonator and (b) the optimized resonator.

3rd bar modes (700 and 1750 Hz, respectively), we note that their presence is weak in the response of the cylindrical resonator compared to the optimized one, where strong coupling occurs. Consequently, the bar decay time for these two modes decreases when using the optimized resonator. Additionally, the feeble presence of the 2nd bar mode on the response of the cylindrical resonator is explained by the fact that its frequency corresponds to an “anti-resonance” of the resonator (between its 2nd and 3rd acoustic modes). A similar effect (albeit weaker) is also seen for the response of the 4th bar mode on the optimized resonator.

To give the reader an audible perspective of the presented results, the sound files associated with the spectrograms in Fig. 10 are provided:

- ‘P(Lr,t)\_cylin.wav’: Resonator response using the cylindrical resonator;
- ‘Y(Lb,t)\_cylin.wav’: Bar response using the cylindrical resonator;
- ‘P(Lr,t)\_optim.wav’: Resonator response using the optimized resonator;
- ‘Y(Lb,t)\_optim.wav’: Bar response using the optimized resonator.

Although only indicative, this example suggests that instruments with multi-modal coupling could lead to a significant increase of sound radiation at multiple frequencies. Additionally, it underlines how the proposed model could be useful in their design and optimization.

## 5. Experimental validation

Several experimental investigations have been carried out to validate different aspects of the developed model. Firstly, we start by exploring the influence of the bar presence on the resonator frequencies. Subsequently, the vibro-acoustic coupling between various beam and resonator modes is studied experimentally and results are compared to modeling predictions, focusing on the influence of the main design parameters: tuning ratio  $\omega_r/\omega_n$ , the bar-resonator distance  $d/a$ , the resonator placement  $x_e$ , and the dissipation ratio  $\zeta_r/\zeta_n$ .

### 5.1. Effect of bar presence on resonator frequencies

Here, we aim to experimentally validate the simplified model for the acoustic radiation impedance of an unflanged pipe with a rigid obstruction, described in Section 2.2.2, and assess how well the geometric simplification of the disk is able to reproduce the presence of actual bars.

The main experimental set-up, shown in Fig. 11(a), consisted of a cylindrical PVC pipe of inner radius  $a = 23$  mm and length  $L_R = 450$  mm ( $a/L_R \simeq 0.05$ ), and an aluminum disk of approximately the same radius (actually  $a = 25$  mm) placed above the resonator open-end. The pipe position was fixed and the disk was supported by a M5 threaded screw, which allowed for a very precise control of the vertical distance  $d$ . Acoustic excitation was provided by a loudspeaker located approximately 300 mm (radial distance) away from open termination of the resonator and the resonator response was measured by an electret microphone located at the closed-end of the pipe. The transfer functions (between excitation signal and the pressure at the end of the resonator) were measured using the exponential sine-sweep method [31]. The test chirp had a duration of 10 s and swept frequencies between 50 Hz and 3 kHz. Subsequently, experimental modal identification was performed using Matlab’s modalfit function [32]. Analogous measurements were made using PVC bars, to investigate potential differences to the simple disk obstruction. At a first instance, the aluminum disk was replaced by a single PVC bar (Fig. 11(b)). Subsequently, three parallel bars were used in an attempt to simulate conditions found in real instruments, where adjacent bars are present, and evaluate if these lead to an added effect (Fig. 11(c)).

The frequencies of the first four acoustic modes were identified, since these fall within the low-frequency approximation assumed

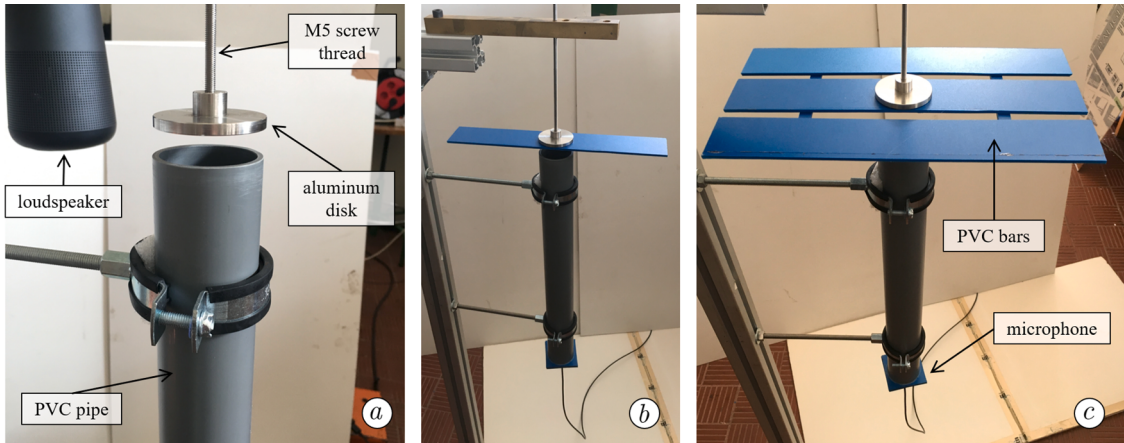


**Fig. 11.** Experimental set-up for the static interaction: (a) disk obstruction; (b) single bar obstruction; (c) triple bar obstruction.

by the proposed model (18), i.e.  $k_r a \approx [0.078, 0.234, 0.389, 0.545]$  (1). Fig. 12 shows results for the identified modal frequencies, at various dimensionless distances  $d/a$ , as well as the analogous results from the proposed model.

Results in Fig. 12 suggest that the presence of the bar (or even a set of three bars) above the resonator can be accurately approximated by the presence of a simple disk of the same radius, as identified frequencies in the three configurations present only minor quantitative differences. No appreciable difference is seen when using either one or three bars. Furthermore, we note that the proposed model is able to describe accurately the behavior observed experimentally. Here, the coefficient  $\eta$  was adjusted to  $\eta = 0.25$ , a value close to our finite-element predictions [15], that had suggested  $\eta \approx 0.32$ .

In realistic scenarios, bars are typically placed at distances between 10 mm and 100 mm above the resonators, hence typically  $0.5 < d/a < 5$ . With that said, results suggest that in real instruments, the frequency of (cylindrical) resonators could be lowered by up to 2%, compared to the frequencies of the unobstructed resonator.

## 5.2. Bar-resonator vibro-acoustic coupling

To assess the validity of the proposed vibro-acoustic model, an experimental apparatus was set-up in an anechoic chamber. The aim was to evaluate the behavior of the coupled-system, both qualitatively and quantitatively, in terms of the most pertinent design parameters: tuning ratio  $\omega_r/\omega_n$ , the dissipation ratio  $\zeta_r/\zeta_n$ , the bar-resonator distance  $d$  and the resonator placement along the bar length  $x_e$ .

As shown in Fig. 13, the set-up was composed of a suspended bar placed over a cylindrical tube of variable length. The tube inner radius was  $a = 25$  mm, and it was composed of two parts connected by a threaded junction, which allowed for a precise variation of its overall length ( $440 \text{ mm} \leq L_R \leq 530 \text{ mm}$ ), and consequently a precise control of the tuning ratio  $\omega_r/\omega_n$ . The acoustic response of the resonator was measured via an electret microphone placed at the closed-end. Additionally, the tube support allowed it to move in the  $x$ -direction, permitting variation of the resonator placement  $x_e$ . The bar used for the main experiments was made of aluminum and was suspended by elastic strings on an appropriate tri-pod mount, which allowed the control of the bar-resonator distance  $d$ . The bar length was  $L_B = 350$  mm and its width equal to the tube diameter  $2a$ . To facilitate measurements of the coupling between various coupled-pairs, the bar was undercut (based on [6]) such that its first four vertical-bending modes are tuned in a ratio (1:3:5:7). Consequently, the flat surface of the bar was faced down to ensure the distance  $d$  is maintained constant along the bar length. The bar was given an impulsive excitation with a small impact hammer (Brüel & Kjær – Type 8203) striking at one end ( $x \approx L_B$ ), while its motion was measured at the other end ( $x \approx 0$ ) using a laser vibrometer (Polytech – PDV100). All three signals were recorded with a Brüel & Kjær Photon data acquisition system.

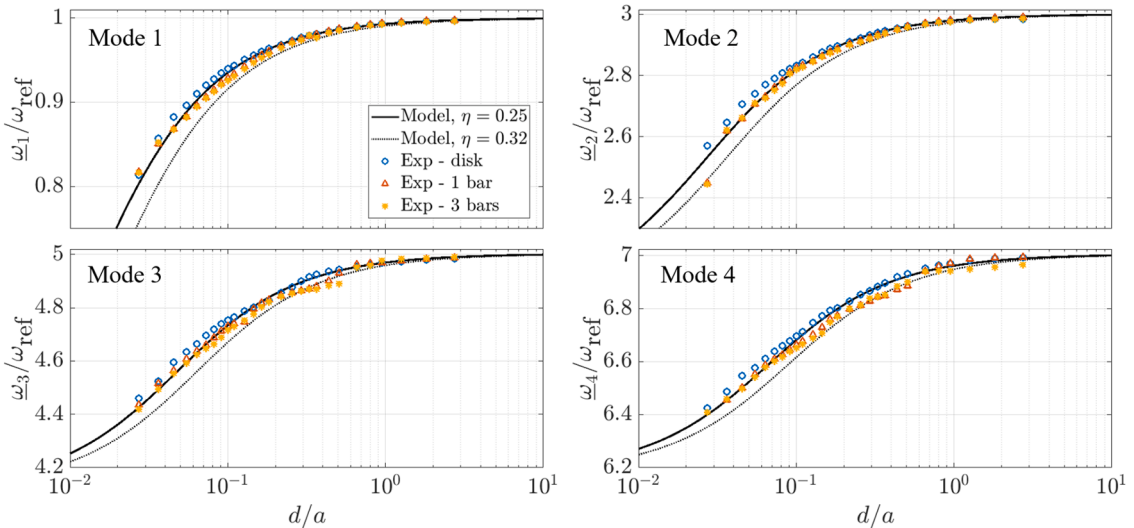


**Fig. 12.** Measured frequencies of the first four resonator modes as a function of the dimensionless distance  $d/a$ , using a disk obstruction (blue), a single bar obstruction (red) and a triple-bar obstruction (yellow). Analogous results from the proposed model with  $\eta = 0.25$  and  $\eta = 0.32$  are shown in black lines (solid and dotted, respectively). The reference frequency was taken as  $\omega_{\text{ref}} = c\pi/(2(L + \Delta L))$ , where  $\Delta L = 0.6133a$  and  $c = 342 \text{ m} \cdot \text{s}^{-1}$ .

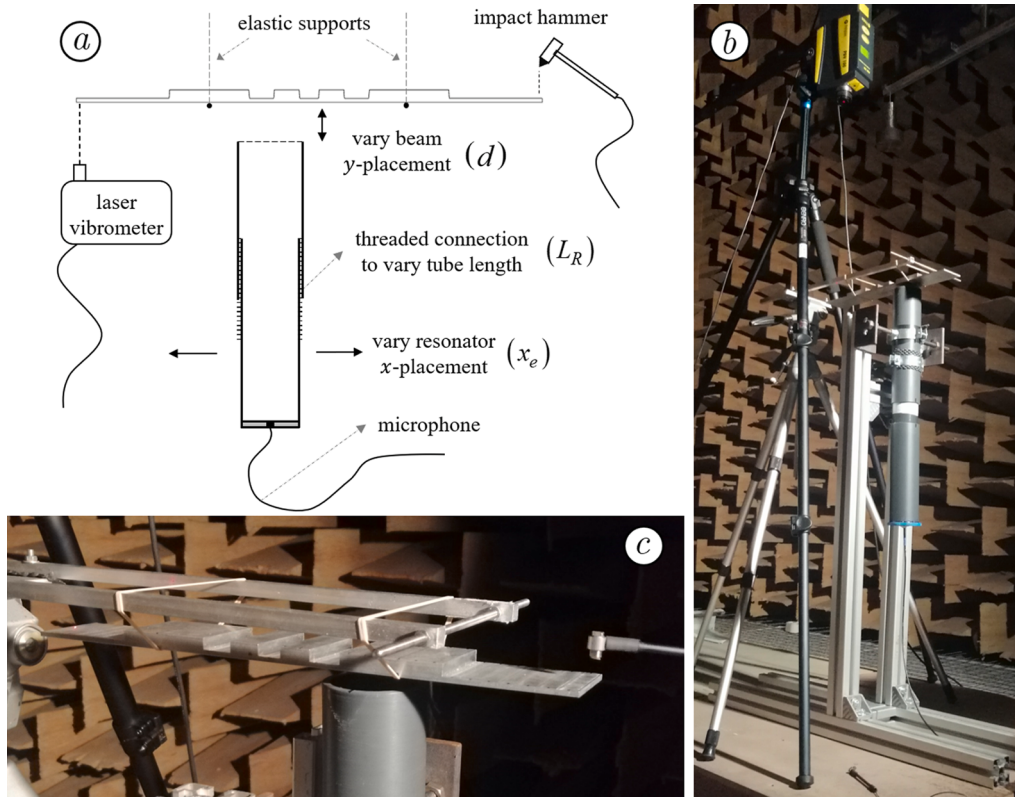


**Fig. 13.** Experimental set-up for the dynamic interaction: (a) schematic description, (b) overview and (c) zoom of the suspended bar and resonator open-end.

#### 5.2.1. Experimental modal identification

Since the main aim was to validate the proposed model, the first step in the experiments was the modal identification of the bar and resonator modes, such that identified modal parameters could be used in the model for comparison. The first four vertical-bending modes of the bar were identified via the measured mobility transfer functions between the force of the impact hammer and the beam-tip velocity. Similarly, the first four resonator modes were identified with the same method described in Section 5.1, for several tube lengths  $L_R$ . To illustrate, Fig. 14 shows two examples of measured and fitted transfer functions for both the bar (left) and the resonator (right).

In both cases, only the modal frequencies ( $\omega_n$ ,  $\underline{\omega}_r$ ) and damping ratios ( $\zeta_n$ ,  $\underline{\zeta}_r$ ) were identified. The considered modal masses ( $m_n$ ,  $m_r$ ) and mode shapes ( $\psi_n(x)$ ,  $\phi_r(y)$ ) were taken from models (for the resonator as described in Section 2.2, and the bar using a finite element model), as these parameters are not particularly easy to measure experimentally and small quantitative differences compared to the modelled values are not expected to change results significantly.

The identified modal parameters are shown in Table 2. The parameters of the resonator are shown in ranges, corresponding to the variations in resonator length. Additionally, Fig. 15 shows the profile of the undercut bar as well as the first four (numerically

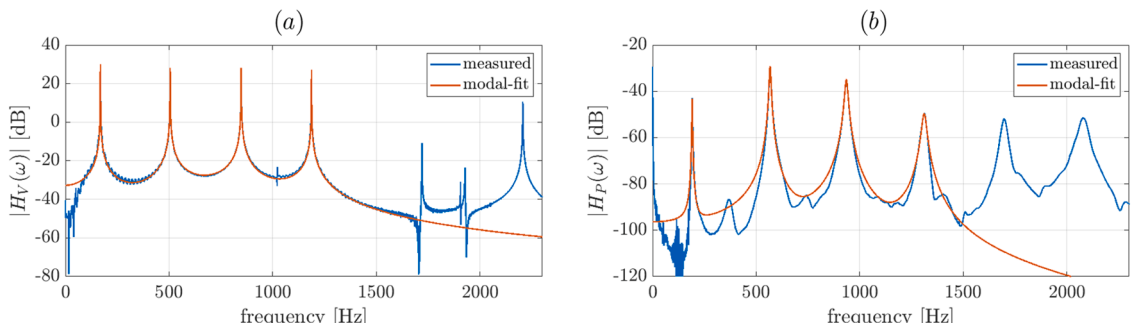


**Fig. 14.** Measured transfer functions and modal-fitting: (a) bar response and (b) resonator response.

**Table 2**

Modal parameters for the first four bar and resonator modes.

$n, r$	Bar			Resonator			
	$\omega_n/2\pi$ (Hz) (measured)	$\zeta_n$ (%) (measured)	$m_n$ (kg) (modelled)	$\underline{\omega}_r/2\pi$ (Hz) (measured)	$\underline{\zeta}_r$ (%) (measured)	$\underline{\zeta}_r$ (%) (modelled)	$\underline{m}_r$ (g) (modelled)
1	168.7	0.0426	0.0450	$173.7 \pm 12.5$	$0.73 \pm 0.04$	$0.10 \pm 0.015$	$0.61 \pm 0.04$
2	505.1	0.0243	0.0307	$507.6 \pm 32.8$	$0.77 \pm 0.04$	$0.28 \pm 0.045$	$0.61 \pm 0.04$
3	847.7	0.0215	0.0241	$845.1 \pm 56.8$	$0.83 \pm 0.06$	$0.46 \pm 0.068$	$0.61 \pm 0.04$
4	1186.6	0.0096	0.0372	$1205.9 \pm 78.6$	$0.94 \pm 0.08$	$0.68 \pm 0.088$	$0.61 \pm 0.04$

calculated) mode shapes  $\psi_n(x)$ .

It is worth underlining that the identified resonator damping ratios  $\underline{\zeta}_r$  are notably larger than those predicted by the model. This difference is not surprising since our model considers dissipation through acoustic radiation only, and neglects visco-thermal losses whose effect is known to be predominant for the lower acoustic modes [30].

### 5.2.2. Effect of tuning ratio, $\underline{\omega}_r/\omega_n$ , and beam-resonator distance, $d/a$

In the first set of measurements, the aim was to measure the decay time  $T_{30,nr}$  and “radiation efficiency”  $\kappa_{nr}$  of different coupled-pairs as a function of the tuning ratio  $\underline{\omega}_r/\omega_n$ . The resonator was maintained centered with the bar  $x_e = L_B/2$ , and measurements were taken for a sweep of discrete tube lengths such that  $0.95 \leq \underline{\omega}_r/\omega_n \leq 1.05$ . Since the bar frequencies are tuned to a ratio close to that of the resonator (1:3:5:7), this procedure allowed for the measurement of all four coupled-pairs at the same time. Additionally, in order to quantitatively validate the proposed vibro-acoustic transfer function  $H(d/a)$ , this procedure was repeated for three bar-resonator distances  $d = [10 \ 20 \ 40]$  mm.

Since the frequencies of all four modes  $\omega_n$  are well separated and damping  $\zeta_n$  is relatively low, the experimentally measured modal (velocity) responses of the bar  $\alpha_n^{\exp}(t)$ , were obtained simply by bandpass filtering the signals of measured velocity  $v^{\exp}(t)$ . Similarly, the modal responses of the resonator  $\gamma_r^{\exp}(t)$  were retrieved from the filtered pressure signals  $p_r^{\exp}(t)$  using the relation (24), leading to

$$\dot{\gamma}_r^{\exp}(t) = -\left(\frac{\underline{\omega}_r}{c}\right) \frac{p_r^{\exp}(t)}{\rho} \quad (45)$$

Subsequently, the modal displacements and velocities,  $\gamma_r^{\exp}(t)$ ,  $\dot{\gamma}_r^{\exp}(t)$  and  $\alpha_n^{\exp}(t)$ , were retrieved through numerical integration. The parameters  $T_{30,nr}$  and  $\kappa_{nr}$  were calculated as in Section 3.2. Note however, that in the experimental case, since damping in the resonator modes is not limited to losses through acoustic radiation, we refrain from using the term “radiation efficiency”  $\kappa_{nr}$ , and replace it by an equivalent term  $K_{nr}$  that describes the percentage of energy lost through generic resonator dissipation (acoustic radiation or other dissipation mechanisms). Nevertheless, the radiation efficiency could eventually be retrieved if we assume that the identified damping ratio  $\underline{\zeta}_r^{\exp}$  is composed of a sum of thermo-viscous losses and radiation losses (modelled), i.e.  $\underline{\zeta}_r^{\exp} = \underline{\zeta}_r^{\text{vis}} + \underline{\zeta}_r^{\text{rad}}$ . Then, the radiation efficiency could be estimated using the modelled values of  $\underline{\zeta}_r^{\text{rad}}$  by

$$\kappa_{nr} = \left( \frac{\underline{\zeta}_r^{\text{rad}}}{\underline{\zeta}_r^{\exp}} \right) K_{nr} \quad (46)$$

Results for the coupling in first and third coupled-pairs are shown in Fig. 16. Note that with  $x_e = L_B/2$ , the coupling of the second and fourth bar modes is bound to be weak since  $\psi_2(x_e) = \psi_4(x_e) = 0$ . For these coupled-pairs, results showed no significant variation of the time decay  $T_{30,nr}$  compared to the uncoupled case, and resonator dissipation  $K_{nr}$  was negligible ( $K_{nr} < 0.5\%$ , for all  $\underline{\omega}_r/\omega_n$ ).

Results in Fig. 16 demonstrate that, qualitatively, the model is able to predict the observed behavior, with the typical decrease in decay time being accompanied by a proportional increase in resonator damping. Moreover, the decrease in coupling strength when the bar is placed further away (larger  $d/a$ ) is also captured by the model. However, quantitatively, the model seems to underestimate the coupling strength in all cases: the decrease in time decays  $T_{30,nr}$  and increase in resonator damping  $K_{nr}$  is always larger in the experimental results. This difference can potentially be attributed to the fact that our vibro-acoustic coupling is based on the disk

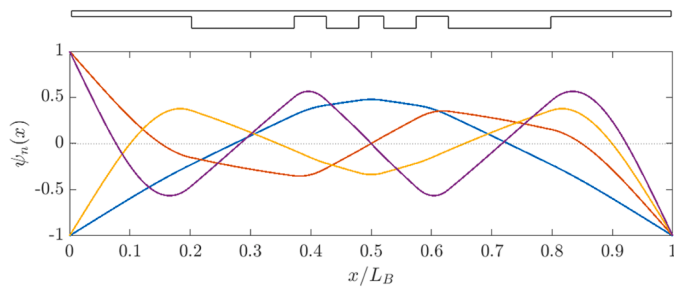
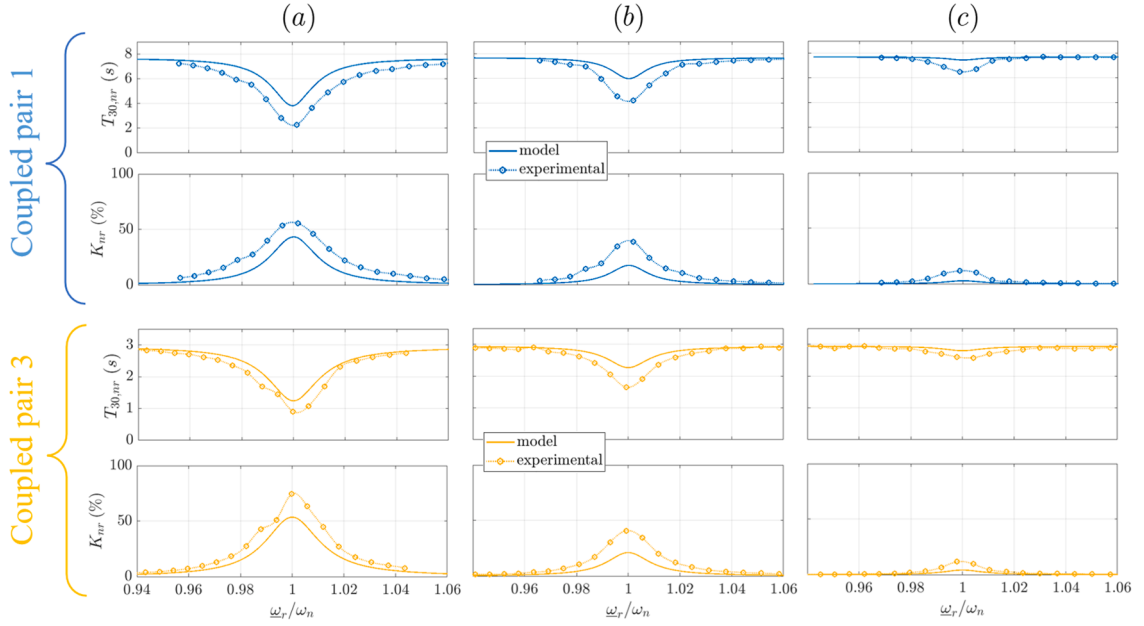


Fig. 15. Profile of the undercut bar (top) and considered modes shapes  $\psi_n(x)$ .



**Fig. 16.** Variation of the decay time  $T_{30,nr}$  (s) and resonator dissipation  $K_{nr}$  (%) as a function of the tuning ratio  $\underline{\omega}_r/\omega_n$ , for three different bar-resonator distances: (a)  $d/a = 0.4$ ; (b)  $d/a = 0.8$ ; and (c)  $d/a = 1.6$ . Top results refer to the first coupled pair ( $n = r = 1$ ), while bottom results refer to the third coupled pair ( $n = r = 3$ ).

geometric simplification, whereby in reality, other regions of the beam will also couple with the resonator acoustics. Additionally, results seem to indicate that this quantitative deviation increases for larger distances  $d/a$ , suggesting the disk simplification is more legitimate when  $d/a$  is smaller. This makes sense for a physical point of view since in the limit  $d/a \rightarrow 0$  the disk simplification should hold. In the appendix, these quantitative deviations are discussed in more detail and an empirical adjustment for the vibro-acoustic model is proposed.

#### 5.2.3. Effect of resonator $x$ -placement, $x_e$

In commercial instruments, resonator pipes are generally placed centered with the bar ( $x_e \approx L_B/2$ ). This is likely the case because coupling is pursued only for the fundamental bar mode, which generally presents large modal displacements at the center. However, the advent of designing instruments with multiple tuned resonator modes, as proposed in [9,10], raises the question of where should the resonator be placed. In this second series of experiments, the distance was fixed at  $d/a = 0.4$ , and the resonator length was fixed such that  $\underline{\omega}_r/\omega_n \approx 1$ , for each coupled-pair. Then, a series of measurements were performed for a sweep of discrete resonator placements in the region  $0.5 \leq x_e/L_B \leq 1$ . Due to bar symmetry, only half the domain was mapped. Results for the decay time  $T_{30,nr}$  and resonator dissipation  $K_{nr}$  are shown in Fig. 17.

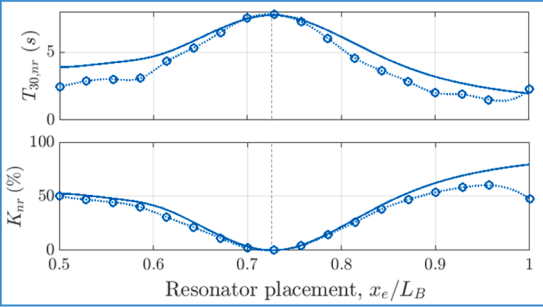
In general, modeling results agree well with the observed behavior, where we see a significant decrease in the coupling strength when the resonator is placed below a nodal line of the bar mode (see Fig. 15). Once again, quantitatively, we notice the model slightly underestimates the coupling strength overall. We also note a slight difference in the shapes of the  $T_{30,nr}$  and  $K_{nr}$  curves, likely due to small differences between the considered and actual mode shapes of the beam (considered modes shapes stem from a 1D Timoshenko beam model). Finally, we notice large differences when the resonator is placed near the tip of the bar  $0.95 \leq x_e/L_B \leq 1$ , in all cases. This deviation is expected since, in these scenarios, the bar does not cover the resonator termination completely (for example, when  $x_e/L_B = 1$ , the bar only covers half the resonator open-end). Here, the disk-assumption naturally leads to an overestimation of the coupling strength.

#### 5.2.4. The case of a highly damped bar, $\underline{\zeta}_r/\zeta_n < 1$

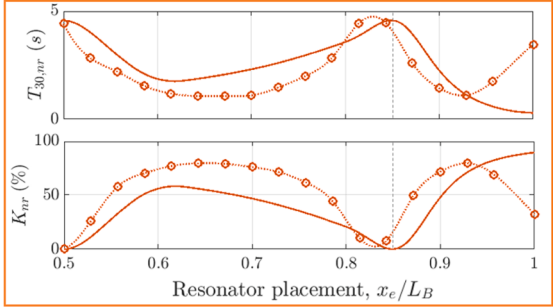
In this third set of measurements, we aimed to explore the curious behavior predicted by the model, whereby a tuned resonator could actually increase decay times  $T_{30,nr}$  as well as resonator dissipation  $K_{nr}$ , in cases where the bar damping is larger than the resonator damping  $\zeta_n > \underline{\zeta}_r$ . For this, a wooden (pine) bar was fabricated in an attempt to achieve a dissipation ratio  $\underline{\zeta}_r/\zeta_n < 1$ . However, the initially measured damping ratio ( $\zeta_n = 0.41\%$ ) did not exceed the large resonator damping measured experimentally ( $\zeta_n \approx 0.73\%$ ). Hence, a plate of PVC was glued to the bar's top in order to increase its modal damping, as shown in Fig. 18.

With the added PVC plate, experimental modal identification of the bar led to:  $\omega_n/2\pi = 159.1$  Hz,  $m_n \simeq 0.044$  kg and  $\zeta_n = 2.08\%$ , where now the dissipation ratio gives  $\underline{\zeta}_r/\zeta_n = 0.346$ . Naturally, this bar is rather artificial and serves only to experimentally validate the behavior predicted by the model. Nevertheless, configurations with  $\underline{\zeta}_r/\zeta_n < 1$ , although rarer, might occur in real instruments as damping ratios of typical wooden bars and resonators tend to fall within the same order of magnitude  $0.1\% < \zeta < 1\%$ . Moreover, the

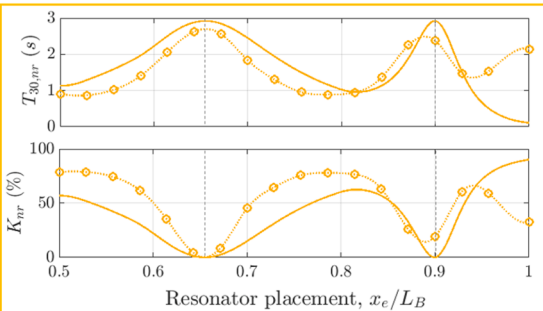
Coupled pair 1



Coupled pair 2



Coupled pair 3



Coupled pair 4

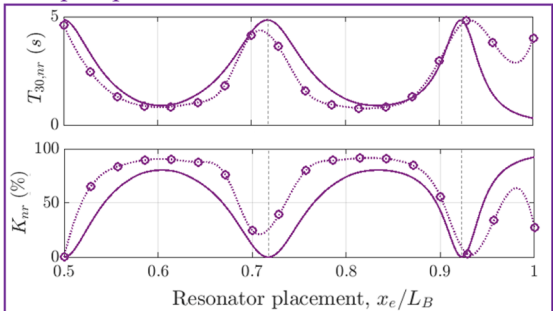


**Fig. 17.** Variation of the decay time  $T_{30,nr}$  (s) and resonator dissipation  $K_{nr}$  (%) as a function of the resonator placement  $x_e$ , for all four coupled-pairs. The distance was fixed at  $d/a = 0.4$  and the tuning ratio  $\omega_r/\omega_n \approx 1$ . The solid lines and circles show the modeling and experimental results, respectively. The vertical dotted lines indicate the location of the nodal points in the bar modes.

analysis of these configurations ( $\zeta_r/\zeta_n < 1$ ) could eventually benefit the design of new instruments, with less orthodox characteristics.

A series of measurements were performed, similar to those described in Section 5.2.2, with  $x_e = L_B/2$ ,  $d/a = 0.4$ , and a sweep of tuning ratios  $\omega_r/\omega_n$ . Results are shown in Fig. 19. In addition to the decay time of the coupled-pair  $T_{30,nr}$ , Fig. 19-(a) also shows the decay time of the isolated bar mode  $T_{30,n}$  (in red), defined by

$$\frac{T_n(T_{30,n}) + U_n(T_{30,n})}{E_{C,nr}(0)} = 0.001 \quad (47)$$

Results demonstrate that indeed, in configurations where  $\zeta_r/\zeta_n < 1$ , a tuned resonator leads to an increase of the decay time of the coupled system. However, the curves of the decay time of the lone bar mode  $T_{30,n}$  show us that the bar *itself* does not vibrate for longer. Actually, its decay time tends to decrease in a tuned scenario (small oscillations in  $T_{30,n}$  are caused by beating effects). Then, an explanation of this behavior becomes more intuitive: in a tuned scenario, the initial vibration of the bar mode will excite the resonator mode efficiently and, because bar damping is larger than that of the resonator, the bar vibration will attenuate quickly while the resonator will continue to vibrate and radiate sound. This phenomenon is illustrated clearly in Fig. 20, showing the energy distribution in the bar and resonator modes in a tuned scenario  $\omega_r/\omega_n \approx 1$ , calculated from measured data.



**Fig. 18.** Wooden bar with an added PVC plate.

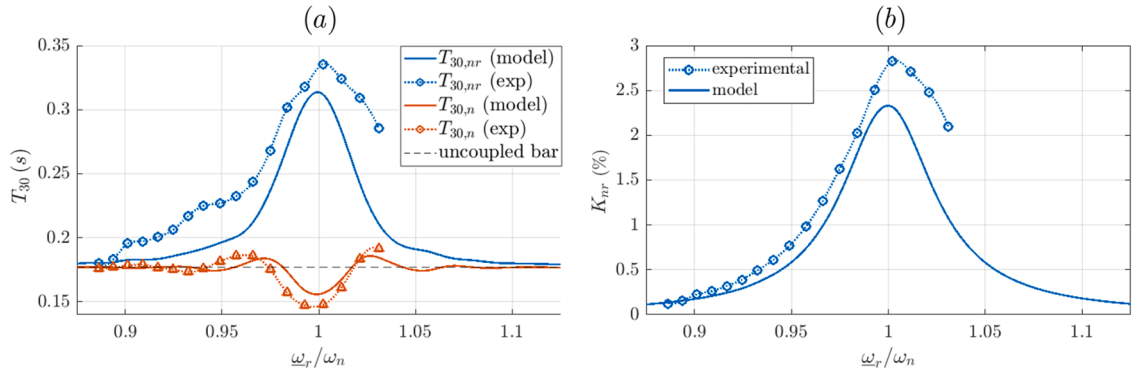


**Fig. 19.** Variations of: (a) the decay time of the coupled-pair  $T_{30,nr}$  and of the lone bar mode  $T_{30,n}$ ; and (b) of the resonator dissipation  $K_{nr}$ (b), as a function of the tuning ratio  $\omega_r/\omega_n$ .

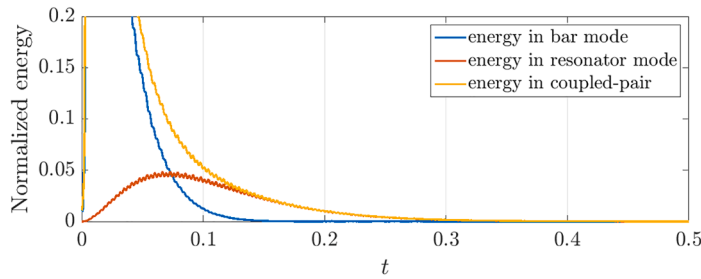


**Fig. 20.** Energy distribution, calculated from measured data, in the bar and resonator modes for a tuned scenario  $\omega_r/\omega_n \approx 1$  with  $\zeta_r/\zeta_n = 0.346$ .

## 6. Conclusions

In this paper we have developed a vibro-acoustic model describing the coupling dynamics between a vibrating beam and an acoustic resonator, as found in mallet percussion instruments like the marimba or the vibraphone. The bar is modelled as a free-free beam, described in a modal framework. Similarly, the resonator is modelled as a cylindrical pipe in terms of its acoustic modes. The vibro-acoustic coupling of the two elements was pursued assuming that only the circular region on the bar just above the resonator will interact with the resonator. The vibro-acoustic transfer function between two parallel disks was used, as developed and validated in a previous work [15]. The proposed formulation led to a simple multi-modal model describing a set of mechanical oscillators (beam modes) inertially coupled to a set of acoustic oscillators (resonator modes).

Experiments were carried out to validate various aspects of the proposed model: (1) change of resonator natural frequencies in the presence of a bar; influence of (2) the tuning ratio  $\omega_r/\omega_n$ , (3) bar-resonator distance  $d$ , (4) resonator placement along the bar length  $x_e$ , and (5) the dissipation ratio  $\zeta_r/\zeta_n$ . The experiments concerning the effect of the bar presence on resonator frequencies compared remarkably well with the proposed model, indicating that in real instruments, the natural frequencies of (cylindrical) pipes can be lowered by up to 2% when a bar is present. Despite some quantitative deviations, the vibro-acoustic model was positively validated by experiments, showing the often-encountered compromise between a decrease of decay time and an increase of acoustic radiation. Additionally, experiments showed that the coupling strength will be severely influenced by the bar mode shape at the location where the resonator is placed  $\psi_n(x_e)$ , namely, a resonator will not couple with a particular bar mode if it is placed directly under a nodal line. Finally, experiments confirmed that in configurations where  $\zeta_r/\zeta_n < 1$  (possibly found in wooden instruments), a tuned resonator will serve to increase both sound radiation and decay time.

The simplicity of the developed lumped-parameter formulation allows for an intuitive understanding of the physical phenomena occurring in real instruments and underlines the main dimensionless parameters affecting its dynamics. This can be a valuable contribution to the design and optimization of modern instruments, especially in the advent of instruments where multiple bar modes are tuned to multiple resonator modes, leading to increased sound radiation at several frequencies. Moreover, with the adequate inclusion of acoustic radiation, this model can serve as a solid basis for sound synthesis, which can be used for the creation of virtual instruments as well as in aiding the design/manufacturing process, by minimizing the construction of prototypes.

## CRediT authorship contribution statement

**Filipe Soares:** Conceptualization, Methodology, Investigation, Validation, Software, Formal analysis, Data curation, Visualization, Writing – original draft, Writing – review & editing. **Vincent Debut:** Investigation, Validation, Supervision, Writing – review & editing. **Jose Antunes:** Supervision, Writing – review & editing.

## Declaration of Competing Interest

The authors have no competing interests.

## Data availability

Data will be made available on request.

## Acknowledgments

The authors gratefully acknowledge the financial support given by “Fundação para a Ciência e Tecnologia” (FCT – Portugal) through the PhD grant referenced SFRH/BD/140598/2018. The authors would also like to thank Prof. José Bento Coelho and Alexandre Pereira from the Centro de Análise e Processamento de Sinais (CAPS) at Instituto Superior Técnico for the access and support at the anechoic chamber. Finally, the authors thank the anonymous reviewers for their many insightful comments and suggestions which ultimately allowed us to improve the quality of the manuscript.

## Supplementary materials

Supplementary material associated with this article can be found, in the online version, at doi:[10.1016/j.jsv.2022.117528](https://doi.org/10.1016/j.jsv.2022.117528).

## Appendix

### *An empirical adjustment of the vibro-acoustic function*

As discussed briefly in [Section 5.2.2](#), the vibro-acoustic model proposed here seems to consistently underestimate the strength of the coupling observed in experiments. Moreover, the (normalized) deviation between the modelled and measured  $T_{30,nr}$  and  $K_{nr}$  curves increases for larger distances  $d/a$ . This seems to indicate that other regions of the beam interact significantly with the resonator and that the disk assumption provides a fair approximation only for small bar-resonator distances. This is not unexpected since, in principle, the disk-assumption should hold in the limit  $d/a \rightarrow 0$ . To quantify these deviations, we have performed numerical integrations where the dimensionless coupling coefficient  $\sigma_{nr}$  was multiplied by  $(A + 1)$ , where  $A$  represents a factor of adjustment of the model, normalized with respect to each particular  $\sigma_{nr}$ . The aim was to find the values  $A^*$  leading to model results that best fitted the experimental curves for the time decay  $T_{30,nr}$ . Results for the best-fitted  $A^*$  are shown in [Table A.1](#) for the first and third coupled-pairs at distances  $d/a = [0.4 \ 0.8 \ 1.6]$ .

The results in [Table A.1](#) quantify the underestimation of the coupling strength in the model. For small distances ( $d/a = 0.4$ ) the underestimation of the coupling is of 98% and 47% for the first and third coupled-pairs, respectively. The value of the underestimation  $A^*$  increases for larger distances  $d/a$ , and for  $d/a = 1.6$ , values go up to 326% and 196%. The last column of [Table A.1](#), shows the value of  $A^*$  normalized by  $d/a$ . Notably, the value of  $A^*/(d/a)$  remains approximately constant for each mode. Starting from the assumption that the disk-simplification is valid in the limit  $d/a \rightarrow 0$ , the above results suggest that a quantitative adjustment of the vibro-acoustic coupling coefficient  $\sigma_{nr}$  could be given for each mode in following form

$$\sigma_{nr}^* = \left[ A_n^* \left( \frac{d}{a} \right) + 1 \right] \sigma_{nr} \quad (\text{A.1})$$

where  $\sigma_{nr}^*$  is the modified coupling coefficients and  $A_n^* = A^*/(d/a)$ , where averaged values for the first and third modes are  $A_1^* = 2.25$  and  $A_3^* = 1.26$ .

It is interesting to note that the normalized adjustment factor  $A_n^*$  is somewhat smaller for the third mode, compared to the fundamental mode. This difference could be attributed to the difference in the bar modal shapes. In the fundamental mode shape  $\psi_1(x)$ , the main anti-node in the central part of the bar (presumably the most influential in the vibro-acoustic coupling) has a larger area than

**Table A.1**

Values of  $A$  leading to the best-fit between modelled and experimental curves, as well as its normalized version  $A/(d/a)$ .

	$d/a$	$A^*$	$A^*/(d/a)$
Coupled-pair 1	0.4	0.98	2.45
	0.8	1.82	2.28
	1.6	3.26	2.03
Coupled-pair 3	0.4	0.47	1.18
	0.8	1.09	1.36
	1.6	1.96	1.23

the equivalent for  $\psi_3(x)$ , where the central region is surrounded by nodal lines, as illustrated in Fig. A.1. It is likely that the latter is more accurately represented by the simplistic disk-assumption. Moreover, the acoustic radiation patterns of higher-order beam modes, where different regions of the beam move in phase opposition, might also contribute to the lower adjustment factor. The results shown in Fig. 17 seem to corroborate these conclusions, as the quantitative deviations between measured and modelled  $T_{30,nr}$  curves decrease for higher-order modes.

To illustrate the effect of the adjustment (Eq. (A.1)), Fig. A.2 compares the previously presented experimental curves for the decay time  $T_{30,nr}$  now compared with results from the adjusted model, using  $A_1^* = 2.25$  and  $A_3^* = 1.26$ .

It is worth underlining that this adjustment, although based on physical considerations, is strictly empirical and is shown here just as a pragmatic method to improve modeling predictions quantitatively. Naturally, the values of  $A_n^*$  will vary according to the nature of the mode shapes of a particular bar. For a more precise account of this effect, three-dimensional models or more extensive experimental investigations are necessary.

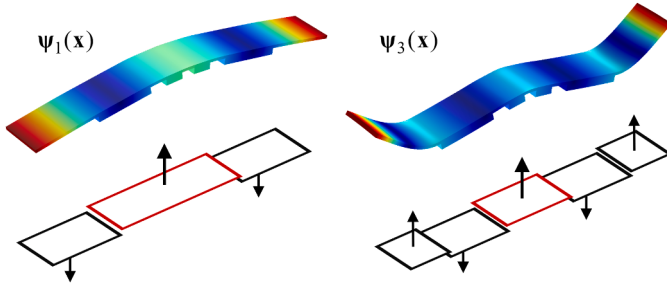


**Fig. A.1.** Three-dimensional illustration of the mode shapes  $\psi_1(x)$  and  $\psi_3(x)$  for the bar used in the experiments and an illustrative schematic representation.

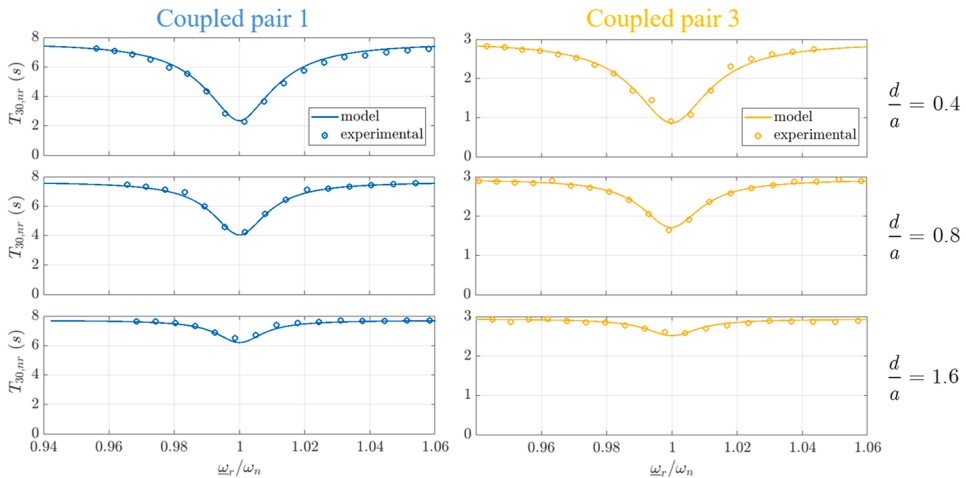


**Fig. A.2.** Time decay  $T_{30,nr}$  as a function of the tuning ratio  $\omega_r/\omega_n$  for the first and third coupled-pairs: comparison between experimental results and the adjusted model, for three dimensionless distances  $d/a = [0.4 \quad 0.8 \quad 1.6]$ .

## References

- [1] L. Henrique, J. Antunes, Optimal design and physical modelling of mallet percussion instruments, *Acta Acust. 89* (2003) 948–963.
- [2] F. Orduna-Bustamante, Nonuniform beams with harmonically related overtones for use in percussion instruments, *J. Acoust. Soc. Am. 90* (6) (1991) 2935–2941.
- [3] F. Soares, J. Antunes, V. Debut, Multi-modal tuning of vibrating bars with simplified undercuts using an evolutionary optimization algorithm, *Appl. Acoust. 173* (2020).
- [4] J. Petrolito, K.A. Legge, Optimal undercuts for the tuning of percussive beams, *J. Acoust. Soc. Am. 102* (4) (1997) 2432–2436.
- [5] D. Beaton, G. Scavone, Three-dimensional tuning of idiophone bar modes via finite element analysis, *J. Acoust. Soc. Am. 149* (6) (2021) 3758–3768.
- [6] F. Soares, J. Antunes, V. Debut, Tuning of bending and torsional modes of bars used in mallet percussion instruments, *J. Acoust. Soc. Am. 150* (4) (2021) 2757–2769.
- [7] D. Beaton, G. Scavone, Experimental measurements of a prototype vibraphone bar with three-dimensional cutaway geometry, *JASA Express Lett. 2* (083201) (2022).
- [8] I. Bork, Practical tuning of xylophone bars and resonators, *Appl. Acoust. 46* (1995) 103–127.

- [9] L. Henrique, O. Inácio, J. Paulino, J. Antunes, Optimization of vibratory and acoustical components of percussion instruments: theoretical and experimental results. *Forum Acusticum*, Budapest, 2005.
- [10] L. Henrique, J. Antunes, O. Inácio, J. Paulino, Application of optimization techniques for acoustical resonators, in: Twelfth International Congress of Sound and Vibration (ICSV12), Lisbon, 2005.
- [11] A. Chaigne, V. Doutaut, Numerical simulations of xylophones. I. Time-domain modeling of the vibrating bars, *J. Acoust. Soc. Am.* 101 (1) (1997) 539–557.
- [12] V. Doutaut, D. Matignon, A. Chaigne, Numerical simulations of xylophones. II. Time-domain modeling of the resonator and the radiated sound pressure, *J. Acoust. Soc. Am.* 104 (3) (1998) 1633–1647.
- [13] P. Rucz, M. Á. Ulveczki, J. Angster, A. Miklós, Simulation of mallet percussion instruments by a coupled modal vibroacoustic finite element method, *J. Acoust. Soc. Am.* 149 (5) (2021) 3200–3212.
- [14] F. Soares, J. Antunes, V. Debut, Simplified model for the bar-resonator vibro-acoustic interaction in mallet percussion instruments, in: 16e Congrès Acoustique Français, Marseille, 2022.
- [15] F. Soares, J. Antunes, V. Debut, A minimal model of the bar-resonator vibroacoustic interaction in mallet percussion instruments, *Appl. Acoust.* 199 (109049) (2022).
- [16] A. Nayfeh, F. Pai, *Linear and Nonlinear Structural Mechanics*, Wiley-VCH, 2004.
- [17] N. Maia, J. Silva, *Theoretical and Experimental Modal Analysis*, Research Studies Press, 2003.
- [18] F. Axisa, J. Antunes, *Modelling of Mechanical Systems: Fluid-Structure Interaction*, Elsevier Ltd., 2007.
- [19] K. Wyckaert, F. Augusztinovicz, P. Sas, Vibro-acoustical modal analysis: reciprocity, model symmetry and model validity, *J. Acoust. Soc. Am.* 5 (100) (1996) 3172–3181.
- [20] S. Hambric, S. Sung, D. Nefske, Interior and exterior sound. *Engineering Vibroacoustic Analysis: Methods and Applications*, Wiley, 2016, pp. 52–69.
- [21] A. Chaigne, J. Kergomard, Dissipation and damping. *Acoustics of Musical Instruments*, Springer-Verlag, New York, 2016, pp. 201–203.
- [22] F. Silva, P. Guillemain, J. Kergomard, B. Mallaroni, A. Norris, Approximation formulae for the acoustic radiation impedance of a cylindrical pipe, *J. Sound Vib.* 322 (2009) 255–263.
- [23] J.L. Favre, "Marimba bar and resonator dimensions for La Favre 5-octave instrument," 2007. [Online]. Available: <http://www.lafavre.us/marimba-bars.htm>. [Accessed 2022].
- [24] A. Chaigne, J. Kergomard, *Acoustics of Musical Instruments*, Springer-Verlag, New York, 2016.
- [25] F. Fahy, Some applications of the reciprocity principle in experimental vibro-acoustics, *Acoust. Phys.* 49 (2) (2002) 217–229.
- [26] T.t. Wolde, Reciprocity measurements in acoustical and mechano-acoustical systems: review of theory and applications, *Acta Acust. United Acust.* 96 (2010) 1–13.
- [27] J. Bensoam, M. Aussal, Self and mutual radiation impedances between translated spheroids. Application to parallel disks, *J. Acoust. Soc. Am.* 150 (2021).
- [28] A. Chaigne, J. Kergomard, Coupled Systems. *Acoustics of Musical Instruments*, Springer-Verlag, New York, 2016, pp. 282–289.
- [29] E. Oliveira, V. Debut, Geometry and tuning assessment of timbals through non-destructive reverse engineering techniques, in: *TecniAcústica 2020*, 2020.
- [30] P. Rucz, J. Angster, A. Miklós, Finite element simulation of radiation impedances with applications for musical instrument design, in: *International Symposium on Music Acoustics (ISMA2019)*, Detmold, Germany, 2019.
- [31] A. Farina, Simultaneous measurement of impulse response and distortion with a swept-sine technique, in: 108th Convention of the Audio Engineering Society, Paris, 2000.
- [32] "MATLAB modalfit: modal parameters from frequency-response functions," Mathworks, [Online]. Available: <https://www.mathworks.com/help/signal/ref/modalfit.html>. [Accessed 10 March 2022].